Space-, Time- and Frequency-Domain Index Modulation for Next-Generation Wireless: A Unified Single-/Multi-Carrier and Single-/Multi-RF MIMO Framework

Chao Xu, *Senior Member, IEEE,* Yifeng Xiong, *Student Member, IEEE,* Naoki Ishikawa, *Member, IEEE,* Rakshith Rajashekar, *Senior Member, IEEE* Shinya Sugiura, *Senior Member, IEEE,* Zhaocheng Wang, *Fellow, IEEE,* Soon-Xin Ng, Lie-Liang Yang, *Fellow, IEEE* and Lajos Hanzo* *Fellow, IEEE*

***Abstract*—As the enabling technolgies move up to the mmWave and even to the TeraHertz bands for the next-generation wireless systems, the signal processing of high-bandwidth orthogonal frequency division multiplexing (OFDM) becomes increasingly power-thirsty, owing to the following OFDM deficiencies: (1) the high peak-to-average power ratio (PAPR); (2) the bandwidth efficiency loss due to the cyclic prefix (CP) overhead; (3) the sensitivity to carrier frequency offset; (4) the complex out-of-band (OOB) filtering. Over the past six decades, a variety of waveforms have been developed in order to mitigate these deficiencies, which are generally achieved at the cost of compromising some of OFDM's beneficial properties, such as its subcarrier (SC) orthogonality, its high throughput and its straighforward adoption to multiple-input multiple-output (MIMO) systems. Against this background, we propose a new waveform termed as multi-band discrete Fourier transform spread-OFDM with index modulation (MB-DFT-S-OFDM-IM), where the component multi-carrier techniques are conceived to constructively function together in order to mitigate the OFDM deficiencies *without compromising the beneficial OFDM properties*. More explicitly, first of all, the PAPR is reduced by the DFT-precoding. Secondly, thanks to the IM design, MB-DFT-S-OFDM-IM is capable of achieving a high throughput that is strictly equal to or higher than the OFDM throughput. Thirdly, MB-DFT-S-OFDM-IM achieves a beneficial frequency diversity gain, which leads to a higher tolerance to carrier frequency offset. Fourthly, the OOB filters are placed in each sub-band before DFT, so that the SC orthogonality remains intact, which is unique to the proposed MB-DFT-S-OFDM-IM structure. Last but not least, we extend the proposed MB-DFT-S-OFDM-IM to support a variety of MIMO schemes, where the IM philosophy is integrated with the space-, time- and frequency-domains within a single *unified* platform.**

***Index Terms*—Index modulation, peak-to-average power ratio, out-of-band, DFT-S-OFDM, frequency-domain equalization, spatial modulation, space-time shift keying, OFDM-IM.**

C. Xu, Y. Xiong, L-L. Yang and L. Hanzo are with the School of Electronics and Computer Science, University of Southampton, Southampton SO17 1BJ, UK (e-mail: {cx1g08,yx8n18,lly,lh}@soton.ac.uk). N. Ishikawa is with the Faculty of Engineering, Yokohama National University, 240-8501 Kanagawa, Japan (e-mail: ishikawa-naoki-fr@ynu.ac.jp). R. Rajashekar is with Broadcom, Bangalore (e-mail: raksh.mysore@gmail.com). S. Sugiura is with the Institute of Industrial Science, University of Tokyo, Meguro-ku, Tokyo 153-8505, Japan (e-mail: sugiura@ieee.org). Z. Wang is with Tsinghua University, Beijing, China (e-mail: zcwang@tsinghua.edu.cn).

The work of N. Ishikawa was supported in part by the Japan Society for the Promotion of Science KAKENHI under Grant 19K14987. The work of S. Sugiura was supported in part by the Japan Society for the Promotion of Science KAKENHI under Grants 26709028 and 16KK0120. The work of S. Sugiura was supported in part by the Japan Society for the Promotion of Science (JSPS) KAKENHI under Grant 16KK0120, Grant 17H03259, and Grant 17K18871 and in part by the Japan Science and Technology Agency (JST) Precursory Research for Embryonic Science and Technology (PRESTO) under Grant JPMJPR1933.L. Hanzo would like to acknowledge the financial support of the Engineering and Physical Sciences Research Council projects EP/N004558/1, EP/P034284/1, EP/P034284/1, EP/P003990/1 (COALESCE), of the Royal Society's Global Challenges Research Fund Grant as well as of the European Research Council's Advanced Fellow Grant QuantCom.

I. Introduction

The classic orthogonal frequency division multiplexing (OFDM) [1]–[3] constitutes the principal waveform of both 4G long-term evolution (LTE) and 5G new radio (NR). The orthogonality of OFDM subcarriers (SCs) facilitates the following benefits: *(A.1)* the robust immunity to frequency-selective multipath effect; *(A.2)* the low-complexity single-tap equalization; *(A.3)* the trivial bandwidth partition; *(A.4)* the straighforward adoption to multiple-input multiple-output (MIMO) systems. Nonetheless, the following OFDM deficiencies are also widely recognized: *(D.1)* the large peak-to-average power ratio (PAPR) that encumbers the power amplifier (PA) design; *(D.2)* the bandwidth efficiency loss due to the cyclic prefix (CP) overhead; *(D.3)* the sensitivity to carrier frequency offset that includes Doppler shift and oscillator mismatch; *(D.4)* the out-of-band (OOB) emission that affects the coexistence of asynchronous users.

Over the past six decades, a variety of waveforms have been developed in order to mitigate the OFDM deficiencies, but they are generally at the cost of compromising some of the key OFDM properties. *Firstly*, in order to reduce the PAPR, the constant envelope OFDM concept was conceived in [4], [5], where non-linear phase modulation is imposed onto the OFDM signal's time-domain (TD) samples. However, as the result of compromising the OFDM orthogonality, the receiver's signal detection complexity is increased and non-linear distortion is inflicted. Moreover, the discrete Fourier transform spread-OFDM (DFT-S-OFDM), which is standardized in the 4G LTE and 5G NR uplink [6], [7], emulates single-carrier transmission that exhibits low PAPR. However, DFT-S-OFDM's rectangular TD pulse leads to a frequency-domain (FD) sinc function that has high side lobes. As a result, a pulse shaping filter that requires excess bandwidth [8] becomes necessary for OOB suppression, which leads to an inevitable loss in bandwidth efficiency. *Secondly*, in order to mitigate the inconsistency in CP lengths, the zero-tail (ZT)

and unique-word (UW) designs [9]–[11] remove the CP usage. Instead, a guard interval is provided by embedding zeros or predefined sequences into the tail of data-carrying OFDM symbols, which leads to enhanced robustness against both time and frequency offset. However, despite eliminating CP, the ZT and UW designs still experience a bandwidth efficiency loss, where the guard interval overhead scales with the tail duration. *Thirdly*, in order to mitigate the OOB emission, the universal filtered multicarrier (UFMC) principle [12]–[15] is often invoked. However, the FD filtering compromises the SC orthogonality, where the OFDM's low-complexity one-tap equalization is replaced by the UFMC's computationally complex matrix inversion that contains the shifted IDFT/DFT matrices as well as the channel impulse response (CIR) matrix.

The recently developed OFDM relying on index modulation (OFDM-IM) has attracted substantial attention [16]–[27]. More explicitly, OFDM-IM partitions N OFDM SCs into G groups, where N_A out of $(N_G = \frac{N}{G})$ SCs are activated in each group. As a result, in addition to the $(GN_A \log_2 L)$ bits that are conveyed by LPSK/QAM symbols, the SC activation index carries extra $(G\lfloor \log_2 \mathcal{C}_{N_G}^{N_A} \rfloor)$ IM bits, where $\mathcal{C}_{N_G}^{N_A}$ refers to the combination of choosing N_A out of N_G. It is proven in [16] that the equivalent SNR on the activated SCs of OFDM-IM is higher than that of OFDM. Nonetheless, the current form of OFDM-IM still has the following limitations. *Firstly*, it was acknowledged in [25]–[27] that the throughput of the original OFDM-IM design cannot compete with that of its OFDM counterparts. In order to improve this, on one hand, the OFDM-IM throughput is further improved in [17]–[21] by optimizing the bit-to-IM mapping, alternating constellation modes and invoking full permutation of the indices. However, the extra dependence imposed among the SCs leads to a substantially increased signal detection complexity at the receiver. *Secondly*, the OFDM-IM performance may be enhanced by transmit diversity techniques including rate reduction, coordinate interleaving and precoding [22]–[24]. Nonetheless, we note that these transmit diversity techniques are not unique to OFDM-IM – they are often routinely invoked in the classic OFDM systems [1]–[3]. *Finally*, despite the fact that a low PAPR was initially advocated as one of the key OFDM-IM advantages [27]–[29], the simple reduction of the number of activated SCs cannot effectively mitigate the multi-carrier PAPR problem. More explicitly, OFDM's TD samples become approximately Gaussian distributed for $N \geq 64$ activated SCs [30]. Accordingly, a reasonable rule of thumb based on the observations in [31] is that OFDM-IM can only exhibit a reduced PAPR, when a very small number of $GN_A \leq 32$ SCs are activated, which imposes a serious limitation on the achievable throughput of OFDM-IM.

It is worth noting that as the enabling technolgies move up from the centimeter Wave (cmWave) band to the millimeter Wave (mmWave) [32]–[35] and even to the TeraHertz band [36]–[38], the high PAPR drawback may outweigh the conventional OFDM benefits in next-generation wireless scenarios. This is due to the fact that the PAs dominate the energy consumption in cellular networks, which contributes as much as 50%∼80% of the power supply at a base station (BS) [39], [40]. Moreover, in the era of 100 Gbps data rates [41], [42], the signal processing of high-bandwidth signals becomes progressively more power-thirsty. However, the maximum achievable efficiency of commercially available PAs remains limited to 20%∼35% [40], [43], where most of the energy is simply dissipated as heat. Furthermore, the PA's dynamic range generally decreases upon increasing the carrier frequency [34]–[36], [40], [43]–[45]. Therefore, processing high-bandwidth high-PAPR OFDM signals becomes increasingly challenging in the mmWave and TeraHertz bands.

Against this background, the following question arises: ***Is it possible to improve OFDM's throughput and BER performance at reduced PAPR and OOB emission without compromising the SC orthogonality?*** In our answer to this question, we propose a new waveform termed as multi-band DFT-S-OFDM with IM (MB-DFT-S-OFDM-IM), which partitions N SCs into G groups of $(N_G = \frac{N}{G})$ SCs. Unlike the conventional OFDM-IM, each group in MB-DFT-S-OFDM-IM forms a sub-band that is precoded by DFT, as seen in Fig. 1. The IM design is invoked either in FD or TD, which constitute FD shift keying (FDSK) and TD shift keying (TDSK) in Fig. 1, respectively. As discussed before, DFT-S-OFDM alleviates OFDM's high-PAPR at the cost of a throughput loss, while OFDM-IM is capable of improving OFDM's throughput and performance at the cost of both high PAPR and increased complexity. By contrast, MB-DFT-S-OFDM-IM is capable of outperforming OFDM at *(I)* a lower PAPR, *(II)* higher throughput, *(III)* frequency diversity gain, *(IV)* improved frequency offset tolerance, *(V)* improved OOB suppression, ***all at the same time, without compromising the OFDM's SC orthogonality***, as explicitly exemplified by Fig. 2. We emphasize here that the performance results of Fig. 2 are definitely not based on cherry-picking the best-performing arrangements of MB-DFT-S-OFDM-IM. Instead, they are from the same set of parameters of MB-DFT-S-OFDM-IM using TDSK associated with $(N = 256)$, $(G \leq 16)$ and QPSK. Moreover, the flexible configuration concerning G can be customized for meeting specific communication requirements. Explicitly, as boldly showcased by Fig. 2, increasing G leads to improvements in throughput, complexity and OOB suppression, but it also results in the gradually increased PAPR and slightly degraded BER. In sumary, the novel contributions are:

1) For MB-DFT-S-OFDM-IM using the FDSK scheme of Fig. 1(a), the M non-zero SCs are evenly partitioned into G groups of $(M_G = \frac{M}{G})$ non-zero SCs, which are precoded by the M_G-point DFT. Moreover, the positions of the remaining $(N_G - M_G)$ idle SCs in each group convey extra IM bits. As a result, MB-DFT-S-OFDM-IM subsumes the existing single-/multi-carrier systems as special cases. Explicitly, $(G = N)$ and $(G = 1)$ conveniently lead to OFDM and DFT-S-OFDM, respectively. Moreover, we have $(N_A = M_G)$ for OFDM-IM, where the DFT is switched off. For a total number of U users, one can either assign $(N_U = N/U)$ SCs to each user as in LTE-style Orthogonal Frequency-Division Multiple Access (OFDMA), or assign each sub-band to a user for Frequency Division Multiple Access (FDMA).

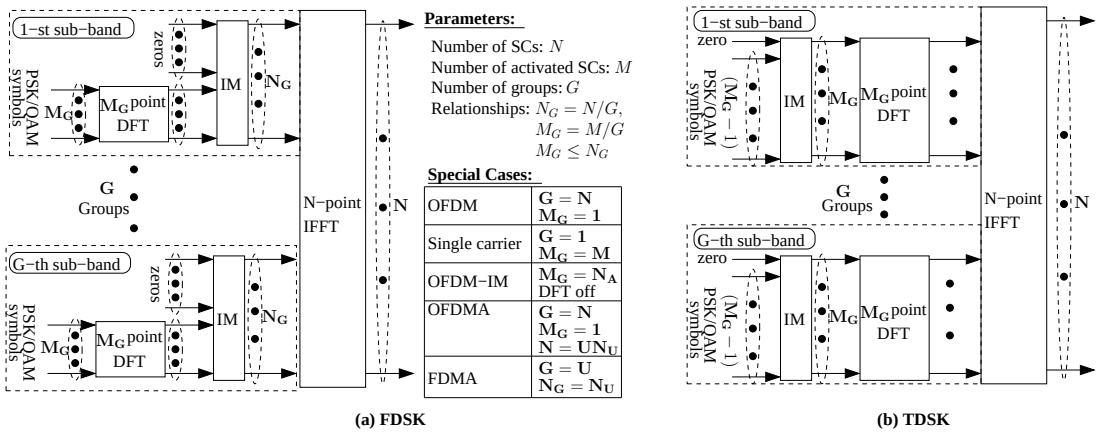

(a) FDSK (b) TDSK

Fig. 1: Generic schematics of the proposed MB-DFT-S-OFDM-IM using FDSK and TDSK.

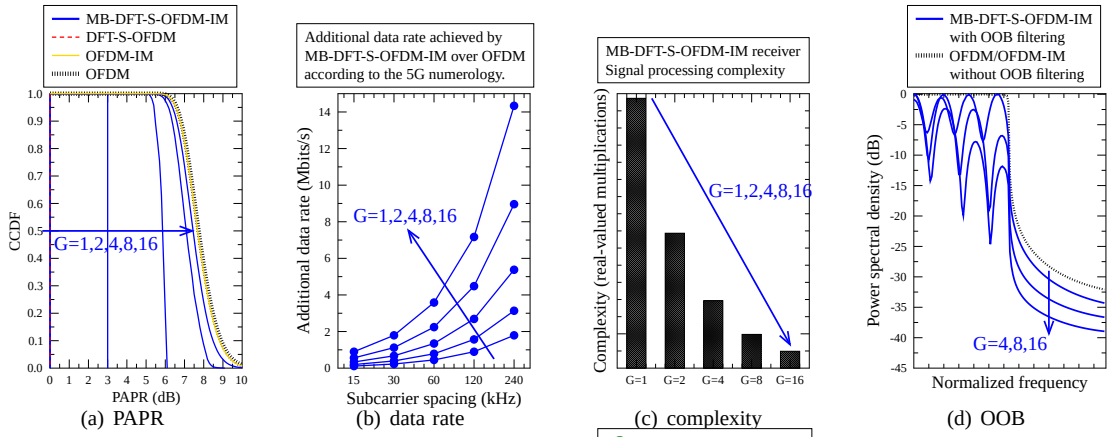

(a) PAPR (b) data rate (c) complexity (d) OOB

(e) BER (f) BER with offset (g) BER with OOB (h) 4×4 V-BLAST

Fig. 2: The performance of the proposed MB-DFT-S-OFDM-IM in terms of PAPR, data rate, complexity and OOB suppression. The detailed descriptions are given in Fig. 5(c), Fig. 6(b), Fig. 7(b), Fig. 11(a), Fig. 8(c), Fig. 12(a), Fig. 11(d) and Fig. 13(d), respectively.

2) However, the SC mapping of FDSK seen in Fig. 1(a) cannot be randomized. Instead, the idle SCs can only be distributed either locally or periodically in the same way as in the DFT-S-OFDM regime [8], [46]–[48], which limits the maximum number of IM bits that can be conveyed. In order to improve this, we propose the TDSK arrangement of Fig. 1(b), so that MB-DFT-S-OFDM-IM becomes capable of achieving a throughput that is strictly equal to or higher than that of OFDM, as exemplified by Fig. 2(b).
3) As the benefit of DFT-precoding, on one hand, the OFDM's PAPR is effectively reduced by decreasing G, as demonstrated by Fig. 2(a). On the other hand, owing to the fact that the DFT-spreading distributes the signal energy uniformly over the SCs, MB-DFT-S-OFDM-IM achieves a beneficial frequency diversity gain, which is sufficient for MB-DFT-S-OFDM-IM to substantially outperform OFDM in the presence of both carrier frequency offset and OOB filtering and in MIMO systems, as exemplified by Figs. 2(e)-(h).
4) Instead of the frequency-domain filtering in the conventional UFMC design [12]–[15], the OOB filtering operation of MB-DFT-S-OFDM-IM is performed in the time-domain before DFT. As a result, the SC orthogonality remains intact, which is unique to the proposed MB-DFT-S-OFDM-IM structure of Fig. 1.
5) Furthermore, MB-DFT-S-OFDM-IM supports *diverse* communication requirements within a single *unified* platform. Conventionally, the MB-DFT-S-OFDM model using no IM is invoked in uplink only, where different

TABLE I: Summary of key notations.

N	number of SCs
G	number of groups
$N_G = \frac{N}{G}$	number of SCs in each group
M	number of non-zero SCs
$M_G = \frac{M}{G}$	DFT size in each group
N_Z	number of idle SCs
$P = \frac{N}{M}$	oversampling ratio
N_h	number of multipath fading components
BPS	number of bits per symbol
$L = 2^{\text{BPS}}$	number of PSK/QAM modulation levels

sub-bands are assigned to different users and there is no benefit in increasing G within the bandwidth assigned for a single user. By contrast, the proposed MB-DFT-S-OFDM-IM is beneficial for both the uplink and downlink, where increasing G leads to flexible trade-off improvements concerning the PAPR, throughput, complexity, OOB radiation as well as BER performance, as exemplified by Fig. 2.

6) Finally, the proposed MB-DFT-S-OFDM-IM is extended to support generic MIMO configurations. Our simulation results demonstrate that the MB-DFT-S-OFDM-IM aided Vertical-Bell Laboratories Layered Space-Time (V-BLAST) scheme is capable of outperforming both its OFDM and OFDM-IM counterparts [49] at a reduced PAPR and an improved throughput. Moreover, the single-carrier special case of MB-DFT-S-OFDM-IM having $(G = 1)$ is adopted for supporting single-RF spatial modulation (SM) [50]–[55] and asynchronous space-time shift keying (ASTSK) [56]–[61]. The ultimate benefit of our new waveform supporting ASTSK is that it is capable of simultaneously gleaning diversity gains in the space-, time- and frequency-domains.

Moreover, as a minor contribution, we conceive a new single-stream ML detection algorithm for OFDM-IM. In contrast to the Log-Likelihood Ratio (LLR) based detector of Basar *et al.* [16], the detection complexity of the proposed algorithm does not increase with the constellation size.

For the sake of clarification, the key notations used in this paper are summarized in Table I. The rest of the paper is organized as follows. MB-DFT-S-OFDM-IM using FDSK and TDSK are conceived in Sec. II, while our case studies including OFDM-IM, uplink DFT-S-OFDM, OOB filtering and carrier frequency offset are discussed in Sec III. The MIMO applications are presented in Sec. IV, and the conclusions are offered in Sec. V.

II. MB-DFT-S-OFDM-IM

A. Design Guidelines

The design guidelines of this paper follow the follwoing two questions. Firstly, can the thoughput of IM compete with that of its multiplexing-oriented and full-rate counterparts? The answer is yes, but it is more realistic to achieve this goal in the FD than in the original spatial domain (SD). To elaborate, it has recently been proven in [62] that for a generalized SM (GSM) scheme activating N_{Tx_A} out of N_{Tx} TAs, the sufficient condition for GSM to have a higher throughput than V-BLAST is $(N_{Tx_A} \geq 2L)$. However, in the most up-to-date 5G standards, only up to four and eight MIMO streams are supported for the uplink and downlink, respectively [6], [7]. The degree of freedom provided by large antenna arrays in mmWave, where numerous half-wavelength-spaced antennas can be accommodated within a compact form, has to be used for beamforming. Hence supporting $N_{Tx_A} \geq 2L$ activated streams is in general unsustainable in the SD. However, in the FD, N_{Tx} and N_{Tx_A} are replaced by the numbers of SCs N and GN_A, where $GN_A \geq 2L$ can be readily satisfied by considering that the number of SCs is often on the order of thousands in modern communication systems.

Secondly, can the IM scheme invoke the single-stream ML detector? In space-/time- domains, the SM and STSK schemes do not impose any inter-channel interference (ICI), hence the single-stream based ML detection is invoked without any performance loss, as demonstrated in [51], [52], [55]. Similarly, thanks to the SC orthogonality in the FD, we will conceive single-stream detectors for both MB-DFT-S-OFDM-IM and OFDM-IM, where no performance loss is imposed, while the detection complexity does not grow with the constellation size.

Moreover, let us clarify the three-fold efficiencies used for characterizing the performance in this paper. ***Bandwidth Efficiency*** is directly quantified by the system throughput, which is the maximum data rate that can be delivered within a given bandwidth. For example, V-BLAST is considered to be a bandwidth-efficient MIMO scheme, because its throughput grows linearly with N_{Tx}. ***Power Efficiency*** refers to the signal transmission power required for achieving a certain target performance. In this scenario, a diversity gain is considered beneficial, which typically leads to a reduction in SNR required for achieving a target BER. ***Energy Efficiency*** takes into account the energy consumption of the transceiver. In a nutshell, the three-fold efficiencies of OFDM including UFMC [12]–[15], DFT-S-OFDM including ZT and UW [9]–[11], OFDM-IM including precoding [16]–[27] and the proposed MB-DFT-S-OFDM-IM are compared in Table II. Specifically, in terms of ***bandwidth efficiency***, both OFDM-IM and MB-DFT-S-OFDM-IM are capable of achieving higher throughput than OFDM, thanks to the IM-based design. Moreover, it is of salient importance for the waveforms to seamlessly support V-BLAST MIMO. In terms of ***power efficiency***, both precoding and DFT-spreading introduce frequency diversity gains, hence the improved BER performance for DFT-S-OFDM, OFDM-IM using precoding and MB-DFT-S-OFDM-IM. Finally, the ***energy efficiency*** is determined by the PAPR at the transmitter, signal detection complexity at the receiver and the ability to support single-/reduced-RF MIMO. In this category, MB-DFT-S-OFDM-IM is capable of achieving a flexibly adjustable low PAPR, of retaining SC orthogonality and of supporting single-/reduced-RF MIMO. Nonetheless, we also have to report that similar to OFDM-IM, MB-DFT-S-OFDM-IM has extra IM detection complexity, which may pose a potential disadvantage. However, thanks to the MB arrangement, the IM detection complexity is reduced by increasing G. Furthermore, the number of IM bits can also be flexibly configured in order to take into account the complexity. These issues are thoroughly investigated in the following sections.

TABLE II: Summary on candidate waveforms.

	Bandwidth efficiency		Power efficiency			Energy efficiency			
	Throughput compared to OFDM	Support V-BLAST MIMO	BER compared to OFDM	BER compared to OFDM (freq. offset)	BER compared to OFDM (OOB filter)	PAPR	Complexity	Complexity (OOB filter)	Support reduce-RF MIMO
OFDM (inc. UFMC)		√				High	SCs orthogonal	SCs non-orthogonal	×
DFT-S-OFDM (inc. ZT/UW)	Lower (pulse shaping)	√	Better	Better	Better	Low	SCs orthogonal		√
OFDM-IM (inc. precoding)	Higher due to IM	√	Better(with precoding)	Better(with precoding)	Better(with precoding)	High	SCs orthogonal (extra IM complexity)	SCs non-orthognal	×
MB-DFT-S-OFDM-IM	Higher due to IM (adjustable with G)	√	Better	Better	Better	Low (adjustable with G)	SCs orthogonal (extra IM comp-lexity adjustable)	SCs orthogonal	√ ($G = 1$)

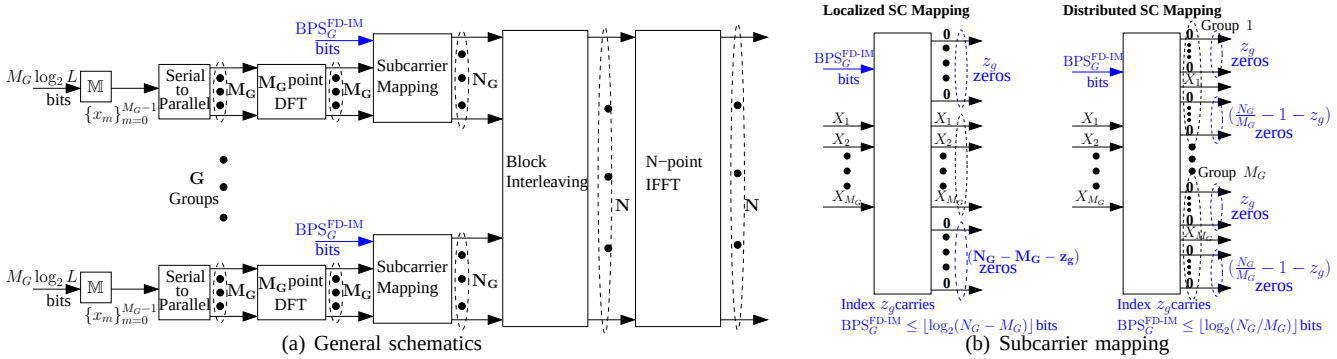

(a) General schematics (b) Subcarrier mapping

Fig. 3: Schematics of the generalized MB-DFT-S-OFDM-IM using FDSK and SC mapping.

B. The FDSK Arrangement

1) MB Signal Generation: The proposed MB-DFT-S-OFDM-IM using FDSK of Fig. 1(a) is detailed in Fig. 3. The N SCs and M non-zero SCs are evenly partitioned into G groups as ($N_G = \frac{N}{G}$) and ($M_G = \frac{M}{G}$), respectively. The total number of zeros is ($N_Z = N - M$) and the oversampling ratio is ($P = \frac{N}{M} = \frac{N_G}{M_G}$). The positions of zeros in each group carry ($\text{BPS}_G^{\text{FD-IM}} = \frac{\text{BPS}^{\text{FD-IM}}}{G}$) IM bits, and the overall throughput is given by ($R = \frac{\text{BPB}}{N}$), where the bits per block (BPB) is given by ($\text{BPB} = M\text{BPS} + \text{BPS}^{\text{FD-IM}}$), and we have ($\text{BPS} = \log_2 L$).

As seen in Fig. 3, in the g-th group, M_G LPSK/QAM symbols $\{x_{g,m}\}_{m=0}^{M_G-1}$ are moduated in the TD. The transmitter performs M_G-point DFT precoding as:

$$X_{g,k} = \frac{1}{\sqrt{M_G}} \sum_{m=0}^{M_G-1} x_{g,m} \omega_{M_G}^{-km}, \tag{1}$$

where $\omega_{M_G} = \exp(j\frac{2\pi}{M_G})$. In order to retain the single-carrier signal for each sub-band, the M_G non-zero SCs have to be distributed either locally or periodically [8], [46]–[48]. On one hand, the localized SC mapping seen in Fig. 3(b) assigns z_g and $(N_G - M_G - z_g)$ zero before and after the M_G contiguous non-zero SCs, where index z_g is capable of conveying $\text{BPS}_G^{\text{FD-IM}} \leq \log_2(N_G - M_G)$ IM bits. The localized SC mapping is represented by:

$$\overline{X}_{g,\overline{k}} = \begin{cases} X_{g,k}, & \text{when } \overline{k} = k + z_g, \\ 0, & \text{otherwise} \end{cases}, \tag{2}$$

where we have $\overline{k} = 0, \cdots, N_G - 1$ and $0 \leq z_g \leq N_G - M_G - 1$. On the other hand, the distributed SC mapping seen in Fig. 3(b) further partitions N_G SCs into M_G groups, where z_g and $(\frac{N_G - M_G}{M_G} - z_g = P - 1 - z_g)$ zeros are assigned before and after the single activated SC in each group, while index z_g conveys $\text{BPS}_G^{\text{FD-IM}} \leq \log_2(P)$ IM bits. The distributed SC mapping is represented by:

$$\overline{X}_{g,\overline{k}} = \begin{cases} X_{g,k}, & \text{when } \overline{k} = kP + z_g, \\ 0, & \text{otherwise} \end{cases}, \tag{3}$$

where $k = 0, \cdots, N-1$ and $0 \leq z_g \leq P - 1$. Following this, the $G \times N_G$ block interleaver [63] is employed as $\overline{X}_{\overline{k}G+g} = \overline{X}_{g,\overline{k}}$.The TD samples are generated by the N-point IFFT as:

$$\overline{x}_n = \sqrt{\frac{P}{N}} \sum_{\widetilde{k}=0}^{N-1} \overline{X}_{\widetilde{k}} \omega_N^{\widetilde{k}n} = \sqrt{\frac{P}{N}} \sum_{g=0}^{G-1} \sum_{\overline{k}=0}^{N_G-1} \overline{X}_{g,\overline{k}} \omega_N^{(\overline{k}G+g)n}, \tag{4}$$

where $\widetilde{k} = \overline{k}G + g$, while the unity TD power $E\{\overline{x}_n\} = 1$ is always ensured.

Proposition 1 (Energy efficiency: PAPR): The TD samples of MB-DFT-S-OFDM-IM are constituted by superpositions of G single-carrier signals, whose PAPR scales with G for $G << N$.

Proof. For the localized SC mapping, (4) may be extended as:

$$\overline{x}_n = \frac{1}{M_G\sqrt{G}} \sum_{g=0}^{G-1} \omega_N^{(z_gG+g)n} \sum_{m=0}^{M_G-1} x_{g,m} f_0'(n - Pm), \tag{5}$$

where $f_0'(n) = \sum_{k=0}^{M_G-1} \omega_{N_G}^{nk} = \omega_{N_G}^{(M_G-1)n/2} \frac{\sin(\frac{\pi n}{P})}{\sin(\frac{\pi n}{N_G})}$ is a circular version of a sinc pulse with zero excess bandwidth, limited to a bandwidth of $\frac{M_G}{N_G T_s}$ [8], [46], [47]. Explicitly, at the integer index of $n_0 = n/P = g_0 M_G + m_0$, the TD sample periodically becomes:

$$\overline{x}_n = \frac{1}{\sqrt{G}} \sum_{g=0}^{G-1} \omega_N^{(z_gG+g)n_0} x_{g_0,m_0}. \tag{6}$$

Simiarly, for the distributed SC mapping, (4) becomes:

$$\begin{aligned} \overline{x}_n &= \sqrt{\frac{P}{M_G N}} \sum_{g=0}^{G-1} \omega_N^{(z_gG+g)n} \sum_{m=0}^{M_G-1} x_{g,m} \sum_{k=0}^{M_G-1} \omega_{M_G}^{k(n-m)} \\ &= \frac{1}{\sqrt{G}} \sum_{g=0}^{G-1} \omega_N^{(z_gG+g)n} x_{g,n \bmod M_G}, \end{aligned} \tag{7}$$

which is also a superposition of G rotated single-carrier signals. As a result, when PSK is employed, the PAPR upper bound is given by G with a probability of occurrence of $(\frac{1}{L})^{G-1}$, where the same modulated PSK phases added constructively at $n = 0$. Similarly, for square QAM signalling, the PAPR upper bound is $\frac{3G(\sqrt{L}-1)}{\sqrt{L}+1}$ with a probability of occurrence of $4\times(\frac{1}{L})^G$ [64]. Based on [30], [31], the superpositioned samples of (6) and (7) become Gaussianized for $G > 32$, which should

be avoided. In summary, for small values of $G << N$, the PAPR of MB-DFT-S-OFDM-IM scales linearly with G. □

2) Bandwidth Efficiency: Based on Proposition 1, increasing G for MB-DFT-S-OFDM-IM leads to a degraded energy efficiency of PAPR. Nonetheless, increasing G would also lead to an improved throughput, subject to the sufficient conditions proven in the Proposition 2 below.

Proposition 2 (Bandwidth efficiency): For MB-DFT-S-OFDM-IM using localized SC mapping, it is sufficient to require $1 \leq G \leq \sqrt{\frac{N}{2}}$, so that the BPB gain obtained from increasing $G > 1$ is strictly non-negative and lower bounded by $\text{BPB}_{\text{Gain}} \geq (G-2)\log_2 G$, which increases monotonically with G. Similarly, for MB-DFT-S-OFDM-IM using distributed SC mapping, it is sufficient to require $G \geq 1$, so that $\text{BPB}_{\text{Gain}} = (G-1)\log_2 P$ also improves with G.

Proof. First of all, for localized SC mapping, the grouping arrangement is only beneficial when the BPB gain is strictly non-negative as $\text{BPB}_{\text{Gain}} = G\log_2 \frac{N_Z}{G} - \log_2 N_Z \geq 0$. This leads to $\log_2 N_Z \geq \frac{G}{G-1}\log_2 G$. Since we always have $\frac{G}{G-1} \leq 2$, it is sufficient to require $G \leq \sqrt{N_Z}$. Let us assume that zero padding is compulsary, which leads to the integer $P > 1$ and hence $N_Z = N - \frac{N}{P} \geq \frac{N}{2}$. Therefore, it becomes sufficient to require $G \leq \sqrt{\frac{N}{2}}$. By using $G \leq \sqrt{N_Z}$, we arrive at $\text{BPB}_{\text{Gain}} \geq (G-2)\log_2 G$. Secondly, for MB-DFT-S-OFDM-IM using distributed SC mapping, we always have a grouping gain, owing to the fact that $G\log_2 \frac{N_G}{M_G} \geq \log_2 \frac{N}{M}$ for $G \geq 1$. This leads to a strictly non-negative $\text{BPB}_{\text{Gain}} = (G-1)\log_2 P$, which also increases monotonically with G. □

3) Single-Stream ML Detection: The signal received at the $\jmath$-th RA is:

$$y_n(\jmath) = \sum_{\tau=0}^{N_h-1} h_\tau(\jmath)\overline{x}_{<n-\tau>_N} + v_n(\jmath), \tag{8}$$

where $< n-\tau >_N$ represents $n-\tau$ modulo N. The multipath components and the additive white Gaussian noise (AWGN) are generated according to $h_\tau(\jmath) \in \mathcal{CN}(0, \frac{1}{N_h})$ and $v_n(\jmath) \in \mathcal{CN}(0, N_{0,TD})$, respectively. Applying N-point FFT at each RA, the FD received signal model is given by:

$$\overline{\mathbf{Y}}_{\widetilde{k}} = \sqrt{P}\overline{X}_{\widetilde{k}}\overline{\mathbf{H}}_{\widetilde{k}} + \mathbf{V}_{\widetilde{k}} \tag{9}$$

where $\overline{\mathbf{Y}}_{\widetilde{k}} = [\overline{Y}_{\widetilde{k}}(0), \cdots, \overline{Y}_{\widetilde{k}}(N_{Rx}-1)] \in \mathbb{C}^{1\times N_{Rx}}$, $\overline{Y}_{\widetilde{k}}(\jmath) = \frac{1}{\sqrt{N}}\sum_{n=0}^{N-1} y_n(\jmath)\omega_N^{-\widetilde{k}n}$, $\overline{\mathbf{H}}_{\widetilde{k}} = [\overline{H}_{\widetilde{k}}(0), \cdots, \overline{H}_{\widetilde{k}}(N_{Rx}-1)] \in \mathbb{C}^{1\times N_{Rx}}$, $\overline{H}_{\widetilde{k}}(\jmath) = \sum_{\tau=0}^{N_h-1} h_\tau(\jmath)\omega_N^{-\widetilde{k}\tau}$, $\overline{\mathbf{V}}_{\widetilde{k}} = [\overline{V}_{\widetilde{k}}(0), \cdots, \overline{V}_{\widetilde{k}}(N_{Rx}-1)] \in \mathbb{C}^{1\times N_{Rx}}$, $\overline{V}_{\widetilde{k}}(\jmath) = \frac{1}{\sqrt{N}}\sum_{n=0}^{N-1} v_n(\jmath)\omega_N^{-\widetilde{k}n}$ and $\overline{X}_{\widetilde{k}} = \frac{1}{\sqrt{N}}\sum_{n=0}^{N-1}\overline{x}_n\omega_N^{-\widetilde{k}n}$. Similar to OFDM-IM, the noise power in FD at the MB-DFT-S-OFDM-IM receiver is reduced to:

$$N_{0,FD} = \frac{N_{0,TD}}{P}. \tag{10}$$

One of the major advantages of the MB-DFT-S-OFDM-IM is that by using the same OFDM framework, the signal processing at the receiver is carried out in the FD, which facilitates the following one-tap MMSE FDE:

$$\overline{U}_{\widetilde{k}} = \frac{1}{\sqrt{P}}\frac{\overline{\mathbf{Y}}_{\widetilde{k}}\overline{\mathbf{H}}_{\widetilde{k}}^H}{\|\overline{\mathbf{H}}_{\widetilde{k}}\|^2 + N_0}, \ 0 \leq \widetilde{k} \leq N-1. \tag{11}$$

This avoids invoking IDFT for all L^{M_G} combinations of $\{x_{g,m}\}_{m=0}^{M_G-1}$. However, the optimal MLSE solution cannot be obtained by the MMSE FDE without further decision feedback [8], [46], [47]. Once again, owing to the SC orthogonality, the proposed DFT-S-OFDM-IM is also free of ICI. Upon obtaining $\overline{U}_{g,k}$ from block de-interleaving, the single-stream based signal detection for the g-th group is summarized as:

Step 1 (SC demapping): $U_{g,k}^{z_g} = \begin{cases} \overline{U}_{g,\overline{k}=k+z_g}, & \text{localized} \\ \overline{U}_{g,\overline{k}=kP+z_g}, & \text{distributed} \end{cases}$.

Step 2 (M_G-point IDFT): $u_{g,m}^{z_g} = \frac{1}{\sqrt{M_G}}\sum_{k=0}^{M_G-1} U_{g,k}^{z_g}\omega_{M_G}^{km}$, $0 \leq m \leq M_G-1$.

Step 3 (Demodulation): $\hat{x}_{g,m}^{z_g} = \mathbb{M}^{-1}(u_{g,m}^{z_g}),\ 0 \leq m \leq M_G-1$.

Step 4 (FD-IM decision): $\hat{z}_g = \arg\ \min_{\forall z_g} \ \sum_{m=0}^{M_G-1} |u_{g,m}^{z_g} - \hat{x}_{g,m}^{z_g}|^2$.

Step 5 (Final decision): $\hat{x}_{g,m} = \hat{x}_{g,m}^{\hat{z}_g},\ 0 \leq m \leq M_G-1$. (12)

There are a total number of $C_G^{\text{FD-IM}} = 2^{\text{BPS}_G^{\text{FD-IM}}}$ candidates for index z_g. Therefore, Steps 1-3 have to be repeated $C_G^{\text{FD-IM}}$ times in order to evaluate $\sum_{m=0}^{M_G-1} |u_{g,m}^{z_g} - \hat{x}_{g,m}^{z_g}|^2$ in Step 4. Moreover, since the IM index z_g is modulated in the FD, it may be detected by:

$$\hat{z}_g = \arg \min_{\forall z_g = 0,\cdots,C_G^{\text{FD-IM}}} \sum_{k=0}^{M_G-1} |U_{g,k}^{z_g} - \frac{1}{\sqrt{M_G}}\sum_{m=0}^{M_G-1}\hat{x}_{g,m}^{z_g}\omega_M^{-km}|^2, \tag{13}$$

where the whole metric of $\{U_{g,m}^{z_g} - \frac{1}{\sqrt{M_G}}\sum_{m=0}^{M_G-1}\hat{x}_{g.m}^{z_g}\omega_{M_G}^{-km}\}$ is the DFT of an error signal $\{e_{g,m} = u_{g,m}^{z_g} - \hat{x}_{g,m}^{z_g}\}$. Therefore, the FDSK's IM index detection is carried out directly in the TD as seen in Step 4 of (12) without invoking the DFT in (13).

Moreover, we note that the single-stream PSK/QAM demodulator is invoked $M_G C_G^{\text{FD-IM}}$ times in Step 3 of (12). For example, when PSK is invoked, the demodulated index is simply given by rounding the angle of $u_{g,m}$ to the nearest PSK phase as $\hat{l}_{g,m} = \lfloor \frac{L}{2\pi}\angle u_{g,m} \rceil$. Similarly, for square QAM, the demodulated index may be obtained by rounding the real and imaginary parts of $u_{g,m}$ to the nearest magnitudes [52]. In summary, the detection complexity order of (12) is given by $\mathcal{O}(M_G C_G^{\text{FD-IM}})$, which does not grow with the constellation size L.

Proposition 3 (Energy efficiency: detection complexity): Although the total number of IM bits is increased with G as $G\text{BPS}_G^{\text{FD-IM}} = G\log_2 \frac{N_Z}{G}$ and $G\text{BPS}_G^{\text{FD-IM}} = G\log_2 P$ for MB-DFT-S-OFDM-IM using localized and distributed SC mapping, respectively, the overall detection complexity order decreases as G grows.

Proof. For MB-DFT-S-OFDM-IM, there are $N_Z = N - M$ zeros in total, but this is reduced to N_Z/G zeros in each group. As a result, the number of IM bits in each group is reduced from $\text{BPS}^{\text{FD-IM}} \leq \lfloor \log_2(N_Z) \rfloor$ to $\text{BPS}_G^{\text{FD-IM}} \leq \lfloor \log_2(N_Z/G) \rfloor$, and the complexity order of (12) is reduced from $\mathcal{O}(MC^{\text{FD-IM}})$ to $\mathcal{O}(GM_G C_G^{\text{FD-IM}})$, where $M = GM_G$. □

Remark 1 (Flexibility on $\text{BPS}_G^{\text{FD-IM}}$): Since the detection complexity order of MB-DFT-S-OFDM-IM using FDSK increases exponentially with $\text{BPS}_G^{\text{FD-IM}}$, it may not always be practical to convey the upper bounds of $\text{BPS}_G^{\text{FD-IM}}$, hence we always denote $\text{BPS}_G^{\text{FD-IM}} \leq \lfloor \log_2(N_G - M_G) \rfloor$ and $\text{BPS}_G^{\text{FD-IM}} \leq \lfloor \log_2(P) \rfloor$ throughout the paper for localized and distributed SC mapping, respectively.

4) Diversity Analysis: The Pairwise Error Probability (PEP) of OFDM-IM has been intensively analysed [63], [65], [66]. However, for the proposed MB-DFT-S-OFDM-IM, the theoretical analysis can only be used for evaluating the diversity

order owing to the following reasons. First of all, MB-DFT-S-OFDM-IM invokes MMSE FDE, which does not reach the MLSE performance without further decision feedback [8], [46], [47]. Secondly, OFDM-IM favours a large value for G that leads to a small value for $(N_G = \frac{N}{G})$, which simplifies the combination design $\mathcal{C}_{N_G}^{N_A}$. By contrast, based on Proposition 1, MB-DFT-S-OFDM-IM requires a small value of $G << N$ that leads to a large $(N_G = \frac{N}{G})$, which prevents us from calculating the PEP by simulation.

Proposition 4 (Power efficiency: diversity order): The frequency diversity order of MB-DFT-S-OFDM-IM using FDSK is given by $r = \min(M_G, N_h)$.

Proof. First of all, the M_G-point DFT of (1) may be formulated in the following matrix form:

$$\mathbf{X} = \frac{1}{\sqrt{M_G}} \sum_{m=0}^{M_G-1} x_m \mathbf{A}_m, \tag{14}$$

where the $(M_G \times M_G)$-element FD signal matrix is represented by the diagonal matrix $\mathbf{X} = \text{diag}(X_{g,0}, X_{g,1}, \cdots, X_{g,M_G-1})$, while the $(M_G \times M_G)$-element equivalent dispersion matrix is given by $\mathbf{A}_m = \text{diag}(1, \omega_{M_G}^{-m}, \cdots, \omega_{M_G}^{-m(M_G-1)})$. The group index g is omitted from (14) for the sake of convenience. The associated distance matrix $\mathbf{\Delta_X} = (\mathbf{X} - \mathbf{X}')(\mathbf{X} - \mathbf{X}')^H$ is of full rank with a non-vanishing determinant of $\det(\mathbf{\Delta_X}) \geq |x_m - x_m'|^{2M_G}$, where the minimum is reached when $x_m \neq x_m'$ and $\{x_{m'} = x_{m'}'\}_{\forall m' \neq m}$. Secondly, after the N-point IFFT at each RA and block de-interleaving, the holistic received signal matrix that contains all N_G SCs of each group may be expressed as:

$$\overline{\mathbf{Y}} = \sqrt{P}\, \overline{\mathbf{X}}\, \overline{\mathbf{H}} + \overline{\mathbf{V}}, \tag{15}$$

where we have $\overline{\mathbf{Y}} = [\overline{\mathbf{Y}}_{g,0}^T, \cdots, \overline{\mathbf{Y}}_{g,N_G-1}^T]^T \in \mathbb{C}^{N_G \times N_{Rx}}$, $\overline{\mathbf{H}} = [\overline{\mathbf{H}}_{g,0}^T, \cdots, \overline{\mathbf{H}}_{g,N_G-1}^T]^T \in \mathbb{C}^{N_G \times N_{Rx}}$ and $\overline{\mathbf{V}} = [\overline{\mathbf{V}}_{g,0}^T, \cdots, \overline{\mathbf{V}}_{g,N_G-1}^T]^T \in \mathbb{C}^{N_G \times N_{Rx}}$. The $(N_G \times N_G)$-element diagonal matrix is given by:

$$\overline{\mathbf{X}}(\overline{k}, \overline{k}) = \begin{cases} \mathbf{X}(\overline{k} - z_g, \overline{k} - z_g), & \text{localized SC mapping} \\ \mathbf{X}[(\overline{k} - z_g)/P, (\overline{k} - z_g)/P], & \text{distributed SC mapping} \end{cases} \tag{16}$$

Based on (15), the PEP may be expressed as:

$$\begin{aligned} p(\overline{\mathbf{X}} \to \overline{\mathbf{X}}') &= E_H \left\{ Q \left[\sqrt{\frac{\|\sqrt{P}(\overline{\mathbf{X}} - \overline{\mathbf{X}}')\overline{\mathbf{H}}\|^2}{2N_0}} \right] \right\} \\ &\leq \left(\frac{P}{4N_0} \right)^{-rN_R} \left[\prod_{\iota=0}^{r-1} \lambda_\iota \right]^{-N_R}, \end{aligned} \tag{17}$$

where $\{\lambda_\iota\}_{\iota=0}^{r-1}$ are the non-zero eigenvalues of the difference matrix $\mathbf{\Delta} = \mathbf{\Delta}_{\overline{X}} \mathbf{\Delta}_{\overline{H}}$. The $(N_G \times N_G)$-element difference matrix $\mathbf{\Delta}_{\overline{X}}$ is a sparse diagonal matrix, where $\text{rank}(\mathbf{\Delta} = \mathbf{\Delta}_{\overline{X}} \mathbf{\Delta}_{\overline{H}})$ is given by the number of non-zero diagonal elements. For the localized SC mapping, we have:

$$\text{rank}(\mathbf{\Delta}_{\overline{X}}) = \begin{cases} M_G, & \text{if } z_g = z_g' \\ M_G + |z - z'|, & \text{if } |z_g - z_g'| \leq M_G \\ 2M_G, & \text{if } |z_g - z_g'| > M_G \end{cases}. \tag{18}$$

Similarly, for the distributed SC mapping, we have:

$$\text{rank}(\mathbf{\Delta}_{\overline{X}}) = \begin{cases} M_G, & \text{if } z_g = z_g' \\ 2M_G, & \text{if } z_g \neq z_g' \end{cases}. \tag{19}$$

Moreover, the second $(N_G \times N_G)$-element matrix in $\mathbf{\Delta}$ is given by $\mathbf{\Delta}_{\overline{H}} = E_H(\overline{H}\overline{H}^H) = \mathbf{W}_{N_G}^H \mathbf{D} \mathbf{W}_{N_G}$, where $\mathbf{W}_{N_G}$ is DFT matrix, while $\mathbf{D}$ has N_h non-zero diagonal elements as $\mathbf{D} = \text{diag}(\frac{1}{N_h}, \cdots, \frac{1}{N_h}, 0, \cdots, 0)$. Therefore, the overall frequency diversity order is given by $r = \text{rank}(\mathbf{\Delta}_{\overline{X}} \mathbf{D}) = \min(M_G, N_h)$. □

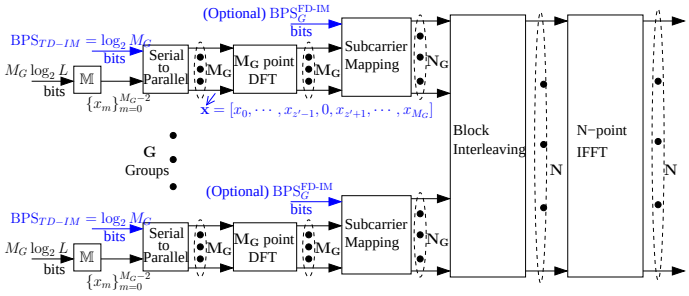

Fig. 4: Schematics of the generalized MB-DFT-S-OFDM-IM using TDSK.

Corollary 1 (Spectral and power efficiencies tradeoff): For MB-DFT-S-OFDM-IM using FDSK associated with $(M_G > 1)$ and $(P > 1)$, the throughput of localized SC mapping is strictly equal to or higher than its distributed SC mapping counterpart. However, based on Proposition 4, the distributed SC mapping is capable of achieving a higher effective frequency diversity gain.

Proof. For $(P \geq 2)$, the range of the DFT size is $2 \leq M_G \leq \frac{N_G}{2}$. Therefore, we have $\text{BPS}_G^{\text{FD-IM}} = \lfloor \log_2(N_G - M_G) \rfloor = \log_2 N_G - 1$ and $\text{BPS}_G^{\text{FD-IM}} = \lfloor \log_2 \left(\frac{N_G}{M_G} \right) \rfloor \in [1, \log_2 N_G - 1]$ for the localized and distributed SC mapping, respectively, where the former is strictly equal to or higher than the latter for $(M_G \geq 2)$. Moreover, based on (18) and (19), the diversity order of $M_G + |z_g - z_g'|$ achieved by a subset of the localized mapped codeword pairs associated with $z_g \neq z_g'$ is lower than $2M_G$ of the distributed counterpart, hence the latter achieves a higher frequency diversity gain over the subset of codewords. □

C. The TDSK Arrangement

The throughput of MB-DFT-S-OFDM-IM using FDSK still cannot compete with OFDM, unless the oversampling ratio $P = \frac{N_G}{M_G}$ is no longer an integer. The smallest $P = \frac{N_G}{N_G - 1}$ corresponds to the case of having a single zero in each group. However, according to Proposition 1, the position of the zero cannot be randomized in the FD, which limits the achievable IM throughput. In order to improve the MB-DFT-S-OFDM-IM throughput, we propose the TDSK arrangement of of Fig. 1(b), which is detailed in Fig. 4. The TDSK of Fig. 4 is similar to the FDSK of Fig. 3, except that the IM aided zero padding is performed in the TD before the DFT precoding as:

$$\mathbf{x}_g = [\, x_{g,1} \; \cdots \; x_{g,z_g'-1} \underset{\downarrow}{z_g'} 0 \; x_{g,z_g'+1} \; \cdots \; x_{g,M_G-1}], \tag{20}$$

where the single zero padding index z_g' conveys $\text{BPS}_G^{\text{TD-IM}} = \log_2 M_G$ bits, while the rest of the $(M_G - 1)$ modulated symbols convey $(M_G - 1)\log_2 L$ bits.

Proposition 5 (Bandwidth efficiency gain over OFDM): It is sufficient to require $M_G = N_G = N/G \geq L$, so that the throughput of MB-DFT-S-OFDM-IM using TDSK becomes $R = \frac{G[\log_2 M_G + (M_G - 1)\log_2 L]}{N}$, which is strictly equal to or higher than the OFDM throughput of $\log_2 L$.

This is significant because it is often assumed that the OFDM-IM throughput cannot compete with that of OFDM [26], [27]. Once again, the MB-DFT-S-OFDM-IM arrangements generally favours small values of $(G << N)$ for the sake of low PAPR, which makes the condition of $M_G = N_G =$

$N/G \geq L$ easy to satisfy. Moreover, we note that the condition of $M_G = N_G$ implies that there is no zero padding in the FD. For this reason, the $\text{BPS}_G^{\text{FD-IM}}$ in the FD is marked as optional in Fig. 4. Without loss of generality, the parameters for the MB-DFT-S-OFDM-IM using TDSK are configured to comply with $M_G = N_G = N/G \geq L$ in the rest of this paper.

Proposition 6 (Bandwidth efficiency gain on G): For MB-DFT-S-OFDM-IM using TDSK, it is sufficient to require $1 \leq G \leq \sqrt{N}$, so that the BPB gain obtained from increasing G is lower bounded by $\text{BPB}_{\text{Gain}} \geq (G-2)\log_2 G$, which grows monotonically with G.

Proof. Similar to Proposition 2, increasing G for MB-DFT-S-OFDM-IM is only beneficial when $\text{BPB}_{\text{Gain}} = G\log_2 \frac{N}{G} - \log_2 N \geq 0$. This leads to the requirement of $\log_2 N \geq \frac{G}{G-1}\log_2 G$, which can be satisfied by $G \leq \sqrt{N}$ because of $\frac{G}{G-1} \leq 2$. As a result, we arrive at $\text{BPB}_{\text{Gain}} \geq (G-2)\log_2 G$. □

Proposition 7 (Energy efficiency: PAPR): The TD samples of the MB-DFT-S-OFDM-IM using TDSK are superpositions of G single-carrier signals, whose PAPR scales with G for $G<<N$.

Proof. After the same DFT precoding $X_{g,k} = \frac{1}{\sqrt{M_G}}\sum_{m=0}^{M_G-1} x_{g,m}\omega_{M_G}^{-km}$ and the block interleaving $\overline{X}_{\overline{k}G+g} = \overline{X}_{g,\overline{k}}$, the N-point IFFT of (4) is extended for MB-DFT-S-OFDM-IM using TDSK as:

$$\begin{aligned}\overline{x}_n &= \sqrt{\tfrac{P_T}{N}}\sum_{g=0}^{G-1}\sum_{\overline{k}=0}^{N_G-1}\overline{X}_{g,\overline{k}}\omega_N^{(\overline{k}G+g)n} \\ &= \sqrt{\tfrac{P_T}{NM_G}}\sum_{g=0}^{G-1}\omega_N^{gn}\sum_{m=0}^{M_G-1}x_{g,m}\sum_{k=0}^{M_G-1}\omega_{M_G}^{(n-m)k} \\ &= \sqrt{\tfrac{P_T}{G}}\sum_{g=0}^{G-1}\omega_N^{gn}x_{g,n \bmod M_G},\end{aligned} \tag{21}$$

which is a superposition of G single-carrier signals as seen in Proposition 1. The normalization $P_T = \frac{M}{M-1}$ ensures unity TD transmission power. □

It is straightforward to see that Proposition 3 on detection complexity and Proposition 4 on the diversity order also apply to the MB-DFT-S-OFDM-IM using TDSK. Furthermore, the the detection procedures of MB-DFT-S-OFDM-IM using TDSK are revised as:

Step 1 (M-point IDFT): $u_{g,m} = \frac{1}{\sqrt{M}}\sum_{k=0}^{M_G-1}U_{g,k}\omega_{M_G}^{km}$, $0 \leq m \leq M_G-1$.
Step 2 (Demodulation): $\hat{x}_{g,m} = \mathbb{M}^{-1}(u_{g,m})$.
Step 3 (TD-IM decision): $\hat{z}'_g = \arg\ \min_{\forall z'_g}\ \|\mathbf{u}_g - \hat{\mathbf{x}}_g^{z'_g}\|^2$.
Step 4 (Final decision): $\hat{\mathbf{x}}_g = \hat{\mathbf{x}}_g^{\hat{z}'_g}$. (22)

Explicitly, $U_{g,k} = \frac{1}{\sqrt{P_T}}\frac{\overline{\mathbf{Y}}_{g,k}\overline{\mathbf{H}}_{g,k}^H}{\|\overline{\mathbf{H}}_{g,k}\|^2+N_0}$ in Step 1 refers to the MMSE FDE output. The $(1\times M_G)$-element matrices in Step 3 are given by $\mathbf{u}_g = [u_{g,0}\ u_{g,1}\ \cdots\ u_{g,M_G-1}]^T$ and $\hat{\mathbf{x}}_g^{z'_g} = [\hat{x}_{g,0}\ \hat{x}_{g,1}\ \cdots\ \hat{x}_{g,M_G-1}]^T$ formulated based on (20) associated with $\hat{x}_{g,z'_g} = 0$. The detection complexity order is given by $\mathcal{O}(M_G)$, which decreases as G grows.

D. Performance Results

Fig. 5 portrays the PAPR trade-off on G. More explicitly, Fig. 5(a) and (b) demonstrate that the PAPR of MB-DFT-S-OFDM-IM using FDSK-localized scale with G for both $N = 256$ and $N = 1024$, respectively. The MB-DFT-S-OFDM-IM using FDSK-distributed and TDSK in Fig. 5(c) and (d) exhibits lower PAPR starting from PAPR=0 dB for $G = 1$ owing to the absence of the FDSK-localized sinc interpolated symbols shown in Proposition 1. Furthermore, Fig. 5(a)-(d) demonstrate that the PAPRs of MB-DFT-S-OFDM-IM are generally lower than those of OFDM-IM and OFDM, but the gap becomes smaller, when increasing G towards 16.

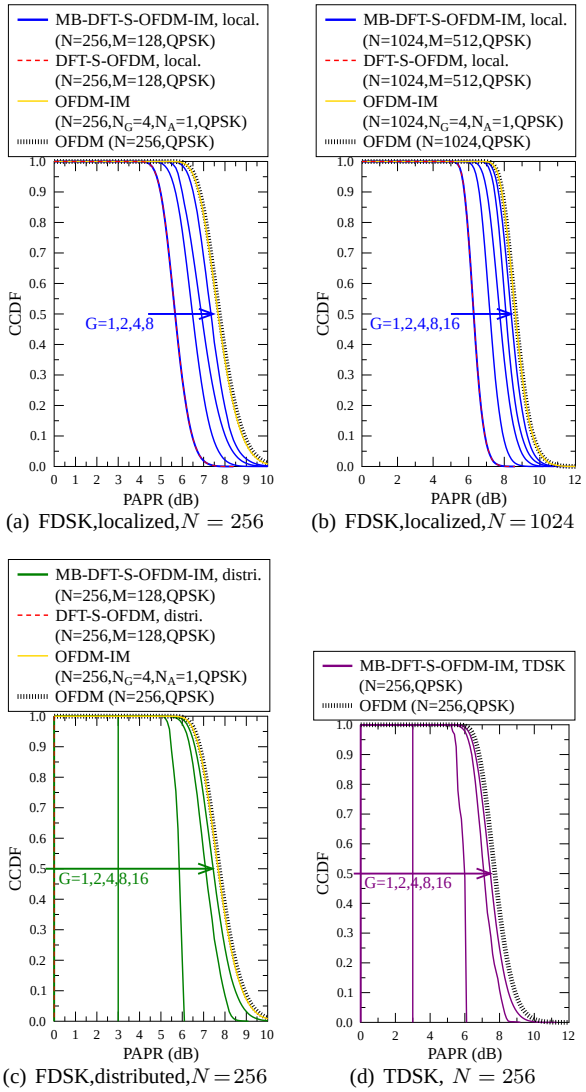

(a) FDSK,localized,$N = 256$ (b) FDSK,localized,$N = 1024$
(c) FDSK,distributed,$N = 256$ (d) TDSK, $N = 256$

Fig. 5: Comparison of CCDFs of PAPRs of the proposed MB-DFT-S-OFDM-IM using FDSK and TDSK, where QPSK is employed. The DFT-S-OFDM, OFDM-IM and conventional OFDM schemes are shown as benchmarks.

Fig. 6 portrays the data-rate gain achieved by the proposed MB-DFT-S-OFDM-IM using FDSK and TDSK over DFT-S-OFDM and OFDM, respectively. This is evaluated based on the 5G numerology [6], [7]. The SC spacing is given by $\text{SCS} = 2^\mu \times 15$ kHz, where $\mu = \{0,1,2,3,4\}$. One slot of 14 OFDM symbols is $2^{-\mu}$ ms for normal CP. Explicitly, Fig. 6(a) confirms Proposition 2 that the data rate of MB-DFT-S-OFDM-IM FDSK increases with G, where the data rate gain over the single-carrier DFT-S-OFDM without IM is evaluated by $2^\mu \times 14 \times (\log_2(\frac{N}{G}) - 1)G \times 10^{-3}$ Mbits/s. Furthermore, Fig. 6(b) confirms Proposition 6 that the data rate of MB-DFT-S-OFDM-IM TDSK also grows with G, where the data rate gain over the full OFDM throughput

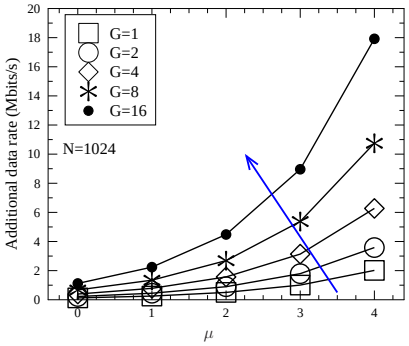

(a) FDSK-localized over DFT-S-OFDM

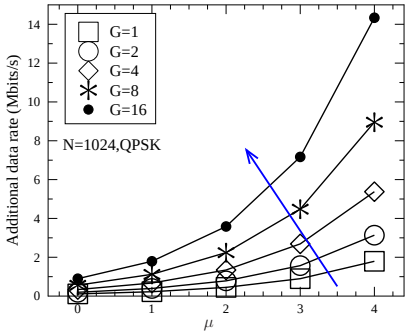

(b) TDSK over OFDM

Fig. 6: The data rate gain of MB-DFT-S-OFDM-IM FDSK over DFT-S-OFDM as well as that of MB-DFT-S-OFDM-IM TDSK over OFDM. The data rate gains of FDSK and TDSK are respectively evaluated by $\left[2^{\mu}\times 14\times \text{BPS}_G^{\text{SCSK}}\times G\times N\times 10^{-3}\right]$ Mbits/s and $\left[2^{\mu}\times 14\times (R-\text{BPS})\times N\times 10^{-3}\right]$ Mbits/s according to the 5G numerology [6], [7].

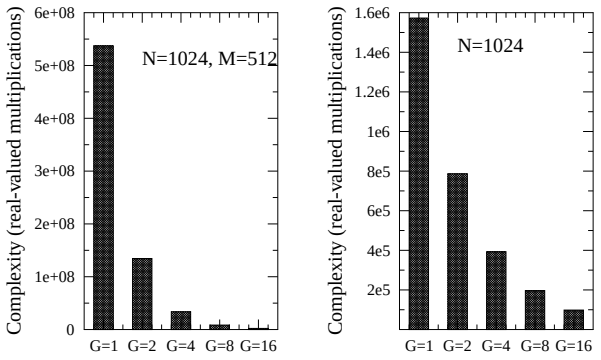

(a) FDSK-localized (b) TDSK

Fig. 7: Complexity (real-valued multiplications) of MB-DFT-S-OFDM-IM using FDSK and TDSK $(N=1024)$.

is given by $2^{\mu}\times 14\times (R-\log_2 L)N\times 10^{-3}$ Mbits/s and $R=\frac{G[\log_2\frac{N}{G}+(\frac{N}{G}-1)\log_2 L]}{N}$ based on Proposition 5.

Fig. 7 presents the detection complexity of MB-DFT-S-OFDM-IM using FDSK and TDSK, which confirm Proposition 3, that the detection complexity indeed decreases as G increases.

Fig. 8 presents our performance comparison between the proposed MB-DFT-S-OFDM-IM using FDSK/TDSK to OFDM-IM and OFDM. We note that performance losses for using $G>1$ in MB-DFT-S-OFDM-IM are recorded in Figs. 8(a)-(d). This is expected because the suboptimal MMSE FDE becomes less reliable as $M_G=M/G$ decreases. Nonetheless, Figs. 8(a)-(d) unequivocally confirm Proposition 4, that the proposed MB-DFT-S-OFDM-IM using FDSK/TDSK are capable of achieving beneficial frequency diversity gains over their OFDM-IM and OFDM counterparts, where the power-efficiency gains are as high as over 10 dB at the BER level of 10^{-4} for $N_{Rx}=1$. This substantial performance improvement is achieved at both a reduced PAPR and an increased BPB, as explicitly indicated in the legends of Figs. 8(a)-(d).

III. Case Studies

A. OFDM-IM

OFDM-IM partitions N SCs into G groups, where N_A out of $N_G=\frac{N}{G}$ are activated as $X_{g,k}=X_{g,k_a}$ for $k\in\mathcal{K}$. The FD indices combination $\mathcal{K}=\{k_a\}_{a=0}^{N_A-1}$ is determined by $\text{BPS}_G^{\text{FD-IM}}=\lfloor\log_2\mathcal{C}_{N_G}^{N_A}\rfloor$ bits, where we have $k_a=0,\cdots,N_G-1$ and $k_a\neq k_{a'}$ for each $\mathcal{K}$. Moreover, each activated SC conveys a modulated LPSK/QAM symbol, hence the overall OFDM-IM throughput is $R=\frac{G(\lfloor\log_2\mathcal{C}_{N_G}^{N_A}\rfloor+N_A\log_2 L)}{N}$. After block interleaver, the TD samples are also generated by the N-point IFFT of (4), and the received signals after N-point FFT are also represented by (9), where P of MB-DFT-S-OFDM-IM may be replaced by $\frac{N_G}{N_A}$ for OFDM-IM. After block de-interleaving, the ML detection may be expressed as:

$$\{\hat{X}_{g,k_a},\hat{\mathcal{K}}_g\}=\arg\min_{\forall\{X_{g,k_a},\mathcal{K}_g\}}\sum_{a=0}^{N_A-1}\|\mathbf{Y}_{g,k_a}-\sqrt{\frac{N_G}{N_A}}X_{g,k_a}\mathbf{H}_{g,k_a}\|^2, \tag{23}$$

which has an excessive complexity order of $\mathcal{O}(2^{\lfloor\log_2\mathcal{C}_{N_G}^{N_A}\rfloor}L^{N_A})$. As a remedy, a near-optimal LLR based detector is conceived in [16], where the LLR associated with each possible activated SC is evaluated and compared. Since the probability evaluations have to visit all L constellation points, the associated detection complexity order is given by $\mathcal{O}(N_G L)$.

In fact, thanks to the SC orthogonality, there is no ICI in OFDM-IM. Therefore, the same single-stream based ML detection principles may also be applied to OFDM-IM. First of all, let us streamline the matrix norm term in (23) as $\|\mathbf{Y}_{g,k_a}-\sqrt{\frac{N_G}{N_A}}X_{g,k_a}\mathbf{H}_{g,k_a}\|^2=(|Z_{g,k_a}-\hat{X}_{g,k_a}|^2-|Z_{g,k_a}|^2)\kappa_{g,k_a}^2$, where we have $Z_{g,k}=\sqrt{\frac{N_A}{N_G}}\mathbf{Y}_{g,k}\mathbf{H}_{g,k}^H/\kappa_{g,k}^2$ and $\kappa_{g,k}^2=\|\mathbf{H}_{g,k}\|^2$. As a result, the OFDM-IM detection is decoupled into the following steps:

$$\begin{aligned}&\textbf{Step 1 (Demodulation):}\ \hat{X}_{g,k}=\mathbb{M}^{-1}(Z_{g,k}).\\&\textbf{Step 2 (IM decision):}\ \hat{\mathcal{K}}_g=\arg\min_{\forall\mathcal{K}_g}\sum_{a=0}^{N_A-1}(|Z_{g,k_a}-\hat{X}_{g,k_a}|^2-|Z_{g,k_a}|^2)\kappa_{g,k_a}^2.\\&\textbf{Step 2 (Final decision):}\ \hat{X}_{g,k_a}=\hat{X}_{g,k}\ \ \forall k_a\in\hat{\mathcal{K}}_g.\end{aligned} \tag{24}$$

The complexity order is reduced to $\mathcal{O}(N_G)$, which does not grow with the alphabet size L. Moreover, owing to the SC orthogonality, the decoupling in (24) always leads to the ML solution.

The BER and complexity comparisons between the sub-optimal LLR detector [16] and the proposed single-stream based ML detector of OFDM-IM are presented in Fig. 9. We note that all the metrics of (24) including $\{Z_{g,k}\}_{k=0}^{N_G-1}$, $\{\kappa_{g,k}\}_{k=0}^{N_G-1}$ and $\{(|Z_{g,k}-\hat{X}_{g,k}|^2-|Z_{g,k}|^2)\kappa_{g,k}^2\}_{k=0}^{N_G-1}$ are evaluated only once. It is evidenced by Fig. 9 that the LLR-based detector imposes a noticeable performance loss in the low-SNR region, while the proposed detector retains the ML performance, despite its substantially reduced complexity that does not grow with L.

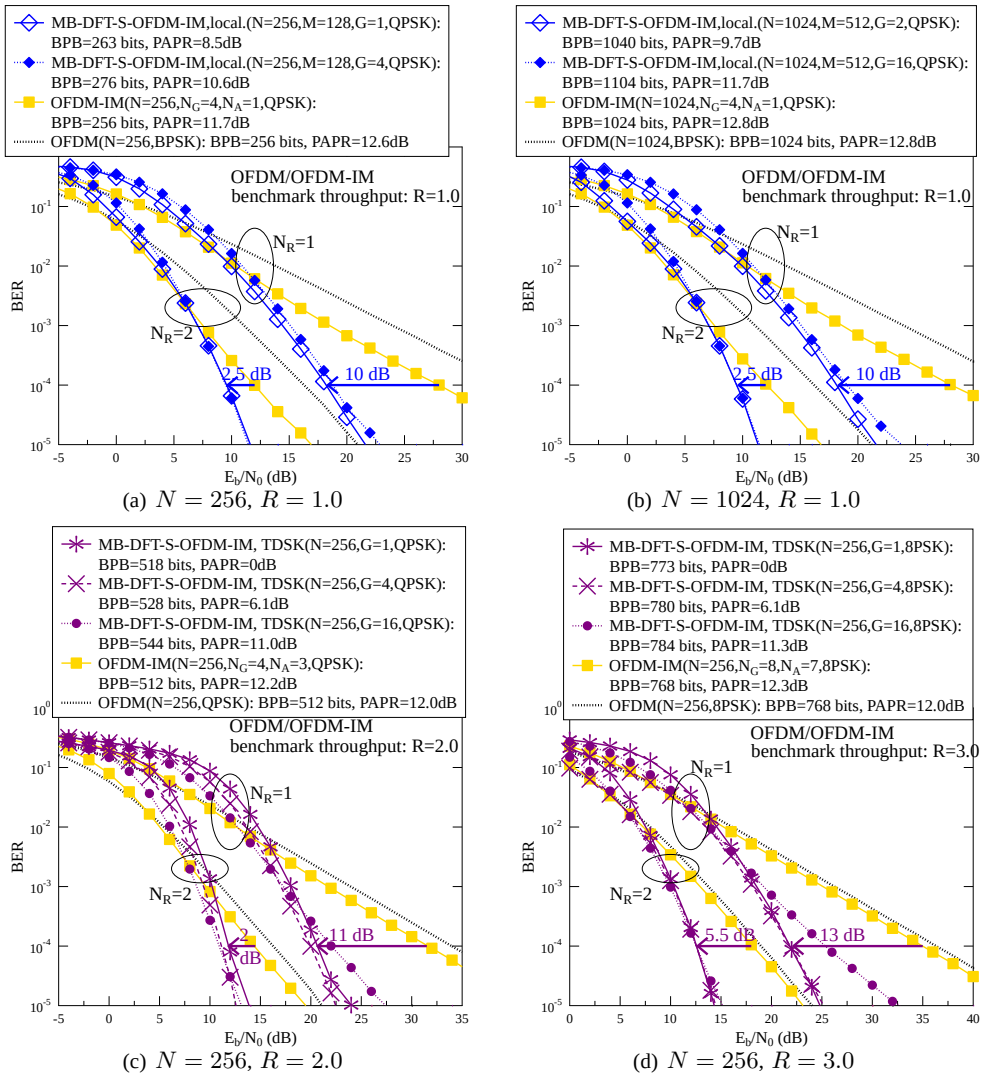

(a) $N = 256$, $R = 1.0$ (b) $N = 1024$, $R = 1.0$

(c) $N = 256$, $R = 2.0$ (d) $N = 256$, $R = 3.0$

Fig. 8: Performance comparison between the proposed MB-DFT-S-OFDM-IM using FDSK and TDSK, where the OFDM-IM and OFDM schemes are presented as benchmarks.

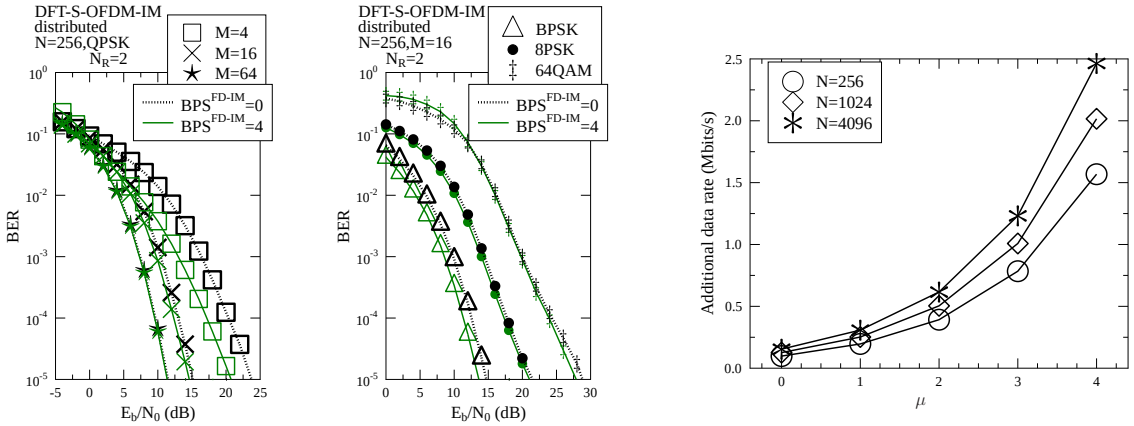

(a) Effect of M (b) Effect of L (c) Data rate gain

Fig. 10: The BER performance gain and data rate gain of the single-carrier DFT-S-OFDM-IM over the conventional single-carrier DFT-S-OFDM (the case of $\text{BPS}^{\text{FD-IM}} = 0$). The data rate gain is evaluated by $2^{\mu} \times 14 \times (\log_2(N) - 1) \times 10^{-3}$ Mbits/s according to the 5G numerology [6], [7].

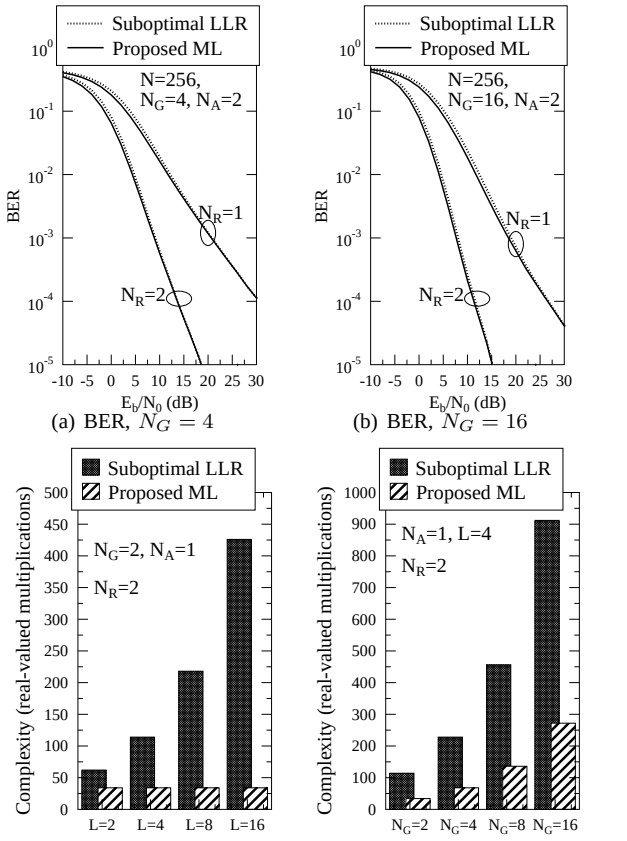

(a) BER, $N_G = 4$ (b) BER, $N_G = 16$

(c) Complexity, effect of L (d) Complexity, effect of N_G

Fig. 9: BER performance and complexity comparison between the sub-optimal LLR detector [16] and the proposed single-stream based ML detector for OFDM-IM.

B. Single-Carrier DFT-S-OFDM-IM

According to Proposition 1, MB-DFT-S-OFDM-IM using FDSK associated with $(G = 1)$, which is termed as DFT-S-OFDM-IM in this section, becomes single-carrier transmission, where the PAPR is exactly the same as that of conventional DFT-S-OFDM, as confirmed by Fig. 5. The advantage of DFT-S-OFDM-IM over DFT-S-OFDM is that IM conveys extra bits in the FD. Figs. 10(a) and 10(b) confirm that the proposed DFT-S-OFDM-IM achieves an improved BER performance over the conventional DFT-S-OFDM. Furthermore, its throughput gain increases substantially with both the SC spacing and N, as evidenced by Fig. 10(c).

C. OOB Filtering

In this section, firstly, we opt for invoking the UFMC [12]–[15], where the filtering operation is applied to a group of SCs. As the number of filters increases to N or reduces to 1, UFMC converges to filter band multicarrier or filtered multicarrier, respectively, which operates either on each SC or on the entire bandwidth [67]. This means that UFMC fits impeccably with the group partitioning in both OFDM-IM and MB-DFT-S-OFDM-IM, where G also becomes the number of filters. More explicitly, the TD samples of (4) are now generated by:

$$\widetilde{\mathbf{x}} = \textstyle\sum_{g=0}^{G-1} \overline{\mathbf{F}}^g \overline{\mathbf{W}}^g \overline{\mathbf{X}}^g = \overline{\mathbf{F}}\ \overline{\mathbf{W}}\ \overline{\mathbf{X}}, \tag{25}$$

where $\overline{\mathbf{X}}^g = [\overline{X}_{g,0}, \cdots, \overline{X}_{g,N_G-1}]^T \in \mathbb{C}^{N_G \times 1}$, while $\overline{\mathbf{W}}^g = \overline{\mathbf{W}}[0 : N-1, gN_G : gN_G + N_G - 1] \in \mathbb{C}^{N \times N_G}$ is the g-th sub-matrix taken from the IDFT matrix $\overline{\mathbf{W}} = \mathbf{W}^H$. The g-th filter matrix $\overline{\mathbf{F}}^g \in \mathbb{C}^{N \times N}$ is a Toeplitz matrix whoes first column contains L_{p} non-zeros taps $[f_1, \cdots, f_{L_{\text{p}}}, 0, \cdots, 0]^T \in \mathbb{C}^{N \times 1}$. Without loss of generality, we opt for invoking a sinc filter with Hamming window, where the low-pass sinc kernel is limited to the $1/G$ bandwidth as $f_l = \frac{2}{G}\text{sinc}(\frac{2}{G}l)$ for the shifted casual index $l = -\frac{L_{\text{tap}}-1}{2}, \cdots, \frac{L_{\text{tap}}-1}{2}$. Furthermore, we have $\overline{\mathbf{X}} = [(\overline{\mathbf{X}}^0)^T, \cdots, (\overline{\mathbf{X}}^{G-1})^T]^T \in \mathbb{C}^{N \times 1}$, $\overline{\mathbf{W}} = \text{diag}(\overline{\mathbf{W}}^0, \cdots, \overline{\mathbf{W}}^{G-1}) \in \mathbb{C}^{GN \times N}$ and $\overline{\mathbf{F}} = [\overline{\mathbf{F}}^0, \cdots, \overline{\mathbf{F}}^{G-1}] \in \mathbb{C}^{N \times GN}$ in (25), where the SC orthogonality is no longer retained, because the IDFT submatrices are shifted in $\overline{\mathbf{W}}$. Following this, the received signals of (8) may be expressed in matrix form as:

$$\mathbf{y} = \widetilde{\mathbf{H}}\widetilde{\mathbf{x}} + \mathbf{v} = \widetilde{\mathbf{H}}_{\text{eff}}\mathbf{X} + \mathbf{v}, \tag{26}$$

where we have $\mathbf{y} = [y_0, \cdots, y_{N-1}]^T \in \mathbb{C}^{N \times 1}$ and $\mathbf{v} = [v_0, \cdots, v_{N-1}]^T \in \mathbb{C}^{N \times 1}$, while $\widetilde{\mathbf{H}} \in \mathbb{C}^{N \times N}$ refers to the circulant CIR matrix. Moreover, the effective channel matrix $\widetilde{\mathbf{H}}_{\text{eff}} = \widetilde{\mathbf{H}}\overline{\mathbf{F}}\ \overline{\mathbf{W}} \in \mathbb{C}^{N \times N}$ has to be equalized as:

$$\overline{\mathbf{U}} = (\widetilde{\mathbf{H}}_{\text{eff}}^H \widetilde{\mathbf{H}}_{\text{eff}})^{-1} \widetilde{\mathbf{H}}_{\text{eff}}^H, \tag{27}$$

which can now be directly invoked by the MB-DFT-S-OFDM-IM receiver of (12), (22) or the OFDM-IM receiver of (24).

It can be clearly seen that (27) of the conventional UFMC has to invoke a $(N \times N)$-size matrix inverse that contains the shifted IDFT matrix, filter matrix and circulant CIR matrix. The associated complexity hinders its applications to large N. Let us recall that the MB-DFT-S-OFDM-IM using TDSK's TD samples of (21) is strictly constituted by G superposition of single-carrier signals. Against this, we propose to apply the OOB filtering in the TD before the DFT precoding of Fig. 4, so that all the SC orthogonalities from the DFT and IFFT at the transmitter to the FFT and IDFT at the receiver remain intact. More explicitly, the TD signals in the g-th group are filtered as:

$$\mathbf{x}'_g = \overline{\mathbf{F}}^g \mathbf{x}_g, \tag{28}$$

where $\mathbf{x}_g = [x_{g,0}, \cdots, x_{g,M_G-1}]^T \in \mathbb{C}^{M_G \times 1}$ are the TD modulated symbols, while the filter matrix $\overline{\mathbf{F}}^g \in \mathbb{C}^{M_G \times M_G}$ is formulated in the same way as defined in (25). Following this, the filtered TD samples $\mathbf{x}'_g = [x'_{g,0}, \cdots, x'_{g,M_G-1}]^T \in \mathbb{C}^{M_G \times 1}$ are the input to the M_G-point DFT of Fig. 4. At the receiver, the equalization is simplied added to Step 1 of (22) as:

$$\mathbf{u}_g = [(\overline{\mathbf{F}}^g)^H \overline{\mathbf{F}}^g]^{-1} (\overline{\mathbf{F}}^g)^H \mathbf{W}_{M_G}^H \mathbf{U}_g, \tag{29}$$

where we have $\mathbf{U}_g = [U_{g,0}, \cdots, U_{g,M_G-1}]^T \in \mathbb{C}^{M_G \times 1}$ and $\mathbf{u}_g = [u_{g,0}, \cdots, u_{g,M_G-1}]^T \in \mathbb{C}^{M_G \times 1}$, while $\mathbf{W}_{M_G} \in \mathbb{C}^{M_G \times M_G}$ is the DFT matrix. It can be seen in (29) that the MB-DFT-S-OFDM-IM receiver only needs to have the *a priori* knowledge of a $(M_G \times M_G)$-size matrix inverse that only contains the filter matrix, which does not need to be updated over time.

Fig. 11(a) portrays the conventional UFMC aided MB-DFT-S-OFDM-IM using TDSK, which evidences the following observations. First of all, the UFMC achieves OOB suppression at the cost of in-band spectrum fluctuations. Secondly, the OOB suppression improves as the number of filter taps L_p and/or the number of filters G increases, which also further deteriorates the in-band spectrum. Moreover, the PSD of Fig. 11(b) demonstrates that the proposed UFMC achieves similar OOB suppressions, yet the in-band spectrum fluctuations appear to be more intense. This is due to the fact that the DFT and IFFT operations at the MB-DFT-S-OFDM-IM transmitter impose phase rotations as seen in (21), which are not taken into account by the filters placed before DFT of (28). Fig. 11(c) confirms the modest performance degradation

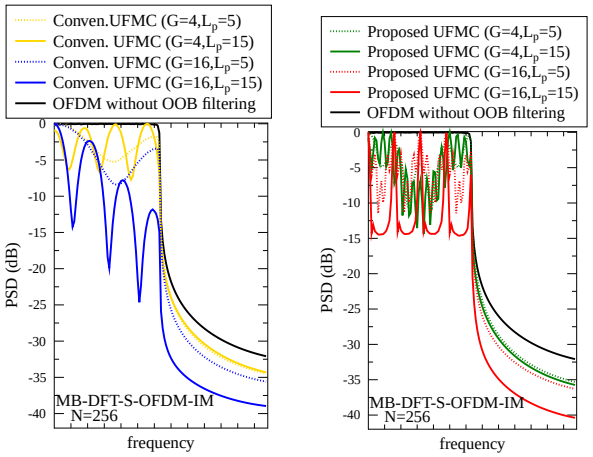

(a) PSD, conventional UFMC (b) PSD, proposed UFMC

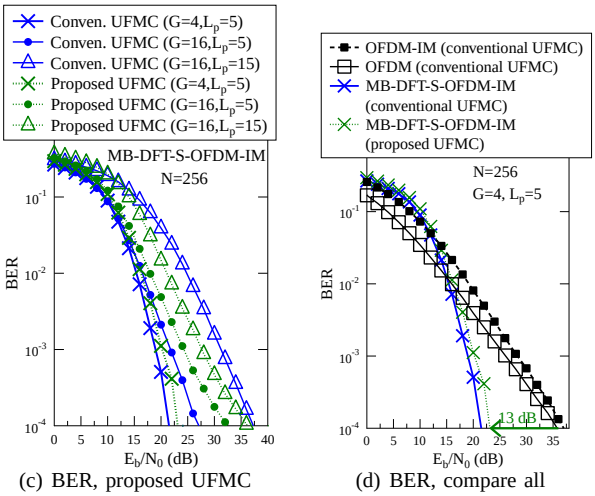

(c) BER, proposed UFMC (d) BER, compare all

Fig. 11: The PSD and BER performance comparison between the conventional and proposed UFMC for MB-DFT-S-OFDM-IM using TDSK. The parameters for OFDM and OFDM-IM are the same as those in Fig. 8(c) associated with $R = 2.0$.

imposed by the proposed UFMC compared to the conventional UFMC. However, Fig. 11(d) further evidences that thanks to the frequency diversity gain, MB-DFT-S-OFDM-IM using the proposed UFMC is still capable of substantially outperforming their OFDM and OFDM-IM counterparts using the conventional UFMC, where a stark 13 dB performance gain is recorded at BER=10^{-4}. Once again, we note that both the conventional and the proposed UFMC can be applied to MB-DFT-S-OFDM-IM, which constitutes an attractive benefit of the new waveform. In contrast, both OFDM and OFDM-IM can only employ the highly complex conventional UFMC.

D. Carrier Frequency Offset

The carrier frequency offset includes Doppler shift and oscillator mismatch, which needs to be estimated and compensated at the receiver. This is particularly difficult for asynchronous uplink transmission [12]–[15], and an accuracy of 1%∼2% of SC spacing is normally required among different users [67]. More explicitly, in the presence of carrier offset, the received signals of (8) is revised in the matrix form as:

$$\mathbf{y} = \widetilde{\mathbf{D}}_d \widetilde{\mathbf{H}} \overline{\mathbf{x}} + \mathbf{v}, \tag{30}$$

where $\overline{\mathbf{x}} = [x_1, \cdots, x_N]^T \in \mathbb{C}^{N\times 1}$ are TD transmitted signals and $\widetilde{\mathbf{H}} \in \mathbb{C}^{N\times N}$ is the circulant CIR matrix, while $\mathbf{y} = [y_0, \cdots, y_{N-1}]^T \in \mathbb{C}^{N\times 1}$ and $\mathbf{v} = [v_0, \cdots, v_{N-1}]^T \in \mathbb{C}^{N\times 1}$ refer to the received signals and the AWGN, respectively. The offset matrix in (30) is given by $\widetilde{\mathbf{D}}_d = \text{diag}[1, \exp(j\frac{2\pi}{N}\Delta f), \cdots, \exp(j\frac{2\pi(N-1)}{N}\Delta f)]$, where Δf is the carrier offset normalized by the SC spacing. Following this, the N-point FFT may be expressed in matrix form as:

$$\mathbf{Y} = \mathbf{W}_N \mathbf{y} = \mathbf{W}_N \widetilde{\mathbf{D}}_d \mathbf{W}_N^H \widetilde{\mathbf{D}}_H \overline{\mathbf{X}} + \mathbf{W}_N \mathbf{v}, \tag{31}$$

where the FD CIR matrix $\widetilde{\mathbf{D}}_H = \mathbf{W}_N \widetilde{\mathbf{H}} \mathbf{W}_N^H$ becomes diagonal, but the offset term $\mathbf{W}_N \widetilde{\mathbf{D}}_d \mathbf{W}_N^H$ is not diagonal, which erodes the SC orthogonality.

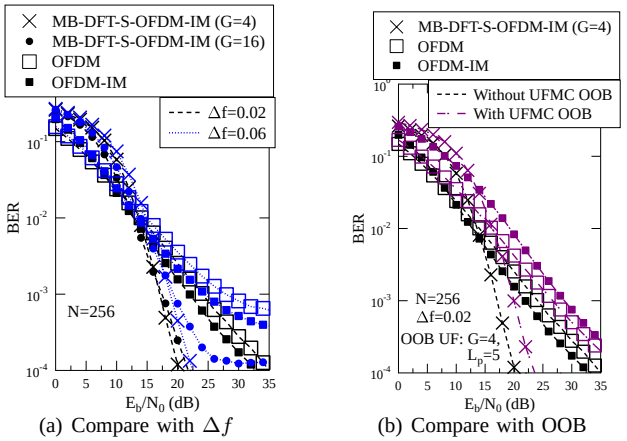

(a) Compare with Δf (b) Compare with OOB

Fig. 12: The BER performance comparison between OFDM, OFDM-IM and the proposed MB-DFT-S-OFDM-IM using TDSK with and without UFMC in the present of carrier frequency offset. The parameters are the same as those in Fig. 8(c) and Fig. 11.

Fig. 12(a) demonstrates that the carrier frequency offset degrades the performance of all multi-carrier schemes, but thanks to the frequency diversity gain, the proposed MB-DFT-S-OFDM-IM ($G = 4$) is capable of tolerating a higher $\Delta f = 6\%$, where their OFDM and OFDM-IM counterparts suffer from error floors. Moreover, it is worthy to note that MB-DFT-S-OFDM-IM associated with an increased ($G = 16$) also experiences an error floor, as seen in Fig. 12(a). This is due to the fact that as discussed in Sec. II, the MMSE FDE is not the MLSE solution, hence a higher G that leads to a smaller N_G in each group tends to degrade the detection reliability. Nonetheless, we note that as previously evidenced by Fig. 8, MB-DFT-S-OFDM-IM associated with ($G = 16$) does not experience error floors in the absence of carrier frequency offset. Moreover, Fig. 12(b) further demonstrates that as expected, UFMC further imposes a performance degradation to all the multi-carrier schemes in the presence of frequency offset, but the proposed MB-DFT-S-OFDM-IM still retains a substantial performance gain over their OFDM and OFDM-IM counterparts.

IV. MIMO Applications

In this section, we opt for extending the proposed MB-DFT-S-OFDM-IM using TDSK of Sec. II-C to support V-BLAST MIMO, because the TDSK arrangement achieves the highest throughput. Moreover, we further invoke the single-carrier DFT-S-OFDM-IM of Sec. III-B to support the single-RF SM and ASTSK.

A. V-BLAST

Considering that MB-DFT-S-OFDM-IM using TDSK is capable of achieving a higher throughput than OFDM, the

proposed V-BLAST MB-DFT-S-OFDM-IM TDSK is capable of achieving a further improved throughput that grows monotonically with the three key parameters, namely with the number of SCs N, the number of MB groups G as well as the number of TAs N_{Tx}.

At the transmitter, each TA independently performs MB-DFT-S-OFDM-IM using TDSK of Sec. II-C. More explicitly, the $(1 \times M_G)$-element modulated symbols of the g-th group at the $\imath$-th TA are given by $\mathbf{x}_g(\imath) = [x_{g,0}(\imath), \cdots, x_{g,M_G-1}(\imath)]$, where the z'_g-th element is zero, while the remaining $(M_G - 1)$ symbols are drawn from the LPSK/QAM constellation. The M_G-point DFT precoding is given by $X_{g,k}(\imath) = \frac{1}{\sqrt{M_G}} \sum_{m=0}^{M_G-1} x_{g,m}(\imath)\omega_{M_G}^{-km}$. Following this, the block interleaver and N-point IFFT are invoked, leading to the TD samples of $\overline{x}_n(\imath) = \sqrt{\frac{P_T}{G}} \sum_{g=0}^{G-1} \omega_N^{gn} x_{g,n \bmod M_G}(\imath)$. The normalization $P_T = \frac{M}{(M-1)N_{Tx}}$ ensures unity transmit power accross N_{Tx} TAs.

The received signals after N-point FFT and block de-interleaving are given by $\mathbf{Y}_{g,k} = \sqrt{P_T}\mathbf{X}_{g,k}\mathbf{H}_{g,k} + \mathbf{V}_{g,k}$, where $\mathbf{Y} \in \mathbb{C}^{1\times N_{Rx}}$, $\mathbf{H} \in \mathbb{C}^{N_{Tx}\times N_{Rx}}$ and $\mathbf{V} \in \mathbb{C}^{1\times N_{Rx}}$ are modelled in the same way as seen in (9). The $(1 \times N_{Tx})$-element V-BLAST signals matrix is given by $\mathbf{X}_{g,k} = [X_{g,k}(0), \cdots, X_{g,k}(N_{Tx} - 1)]$. The MMSE FDE is given by $\mathbf{U}_{g,k} = \mathbf{Y}_{g,k}\overline{\mathbf{G}}_{\text{MMSE}}$, where $\overline{\mathbf{G}}_{\text{MMSE}} = \frac{1}{\sqrt{P_T}}(\overline{\mathbf{H}}_{g,k}^H\overline{\mathbf{H}}_{g,k} + N_{Tx}N_0\mathbf{I}_{N_R})^{-1}\overline{\mathbf{H}}_{g,k}^H$. As a result, the ICIs are completely eliminated from the detection of $\|\mathbf{U}_{g,k} - \mathbf{X}_{g,k}\|^2 = \sum_{\imath=0}^{N_{Tx}-1} |U_{g,k}(\imath) - X_{g,k}(\imath)|^2$, which may be decoupled for signal detection of each TA. More explicitly, the single-stream based V-BLAST MB-DFT-S-OFDM-IM TDSK detection is summaried as follows:

$$
\begin{aligned}
&\textbf{Step 1 } (M_G\text{-point IDFT}): && u_{g,m}(\imath) = \tfrac{1}{\sqrt{M}} \textstyle\sum_{k=0}^{M_G-1} U_{g,k}(\imath)\omega_{M_G}^{km}.\\
&\textbf{Step 2 } (\text{Demodulation}): && \hat{x}_{g,m}(\imath) = \mathbb{M}^{-1}(u_{g,m}(\imath)).\\
&\textbf{Step 3 } (\text{TD-IM decision}): && \hat{z}'_g(\imath) = \arg\min_{\forall z'_g} \|\mathbf{u}_g(\imath) - \hat{\mathbf{x}}_g^{z'_g}(\imath)\|^2.\\
&\textbf{Step 4 } (\text{Final decision}): && \hat{\mathbf{x}}_g(\imath) = \hat{\mathbf{x}}_g^{\hat{z}'_g}(\imath).
\end{aligned}
\tag{32}
$$

We have $\mathbf{u}_g(\imath) = [u_{g,0}(\imath)\ u_{g,1}(\imath)\ \cdots\ u_{g,M_G-1}(\imath)]$ and $\hat{\mathbf{x}}_g^{z'_g}(\imath) = [\hat{x}_{g,0}(\imath)\ \hat{x}_{g,1}(\imath)\ \cdots\ \hat{x}_{g,M_G-1}(\imath)]$ associated with $\hat{x}_{g,z'_g}(\imath) = 0$. The detection complexity order is given by $\mathcal{O}(N_{Tx}M_G)$.

Fig. 13 portrays our performance comparison between the V-BLAST using the proposed MB-DFT-S-OFDM-IM TDSK scheme as well as its OFDM-IM and OFDM counterparts. The low-complexity linear MMSE FDE is invoked for V-BLAST MB-DFT-S-OFDM-IM TDSK. Similarly, the linear MMSE detector is invoked for OFDM-IM and OFDM. Once again, we note that the performance difference between $(G = 1)$ and $(G = 8)$ of MB-DFT-S-OFDM-IM seen in Figs. 13(a)-(d) is due to the sub-optimal MMSE FDE, which is not the MLSE solution. Nonetheless, the performance loss imposed by increasing G is negligible compared to the performance improvements of MB-DFT-S-OFDM-IM over OFDM-IM, which are well over 10 dB at the BER level of 10^{-4} in Figs. 13(a)-(d). Once again, the performance advantages of the proposed MB-DFT-S-OFDM-IM TDSK over its OFDM-IM and OFDM counterparts seen in Figs. 13(a)-(d) are achieved at both a reduced PAPR and an increased BPB.

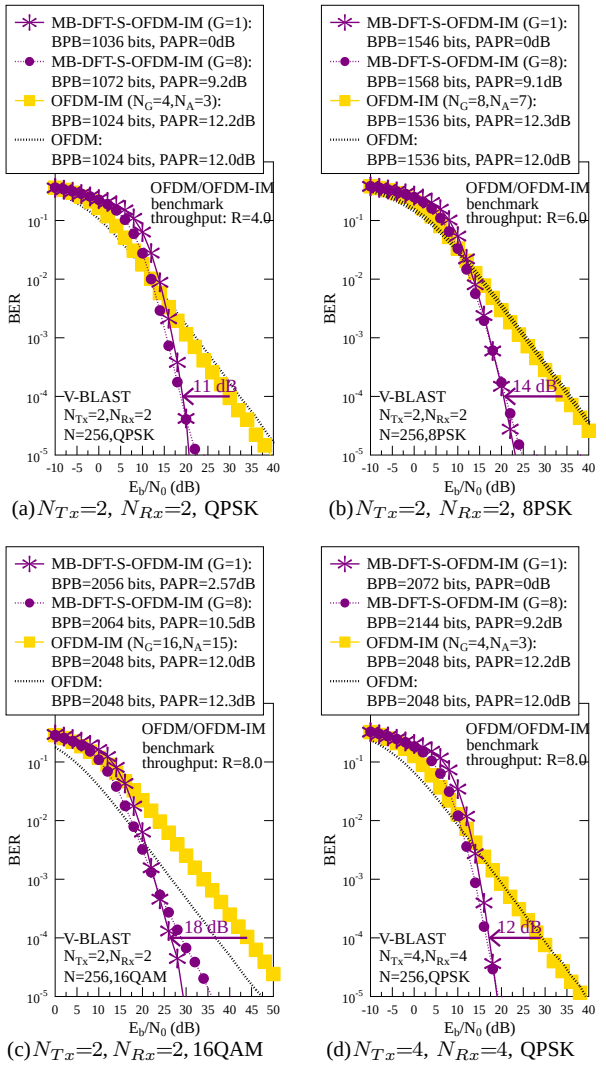

(a) N_{Tx}=2, N_{Rx}=2, QPSK (b) N_{Tx}=2, N_{Rx}=2, 8PSK

(c) N_{Tx}=2, N_{Rx}=2, 16QAM (d) N_{Tx}=4, N_{Rx}=4, QPSK

Fig. 13: Performance results of V-BLAST using the proposed MB-DFT-S-OFDM-IM TDSK as well as the OFDM-IM and OFDM schemes.

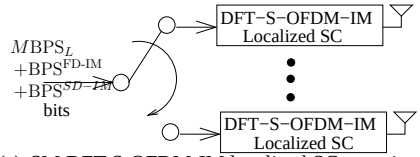

(a) SM DFT-S-OFDM-IM,localized SC mapping

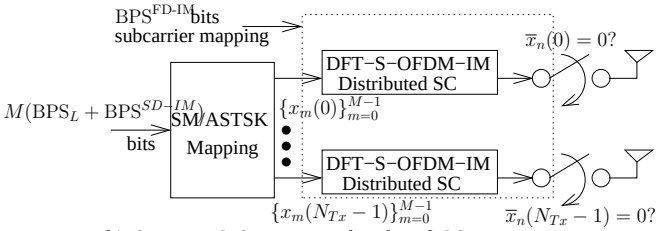

(b) SM DFT-S-OFDM-IM, distributed SC mapping

Fig. 14: Schematics of single-carrier DFT-S-OFDM-IM aided single-RF SM.

B. SM and ASTSK

Based on Proposition 1 associated with $(G = 1)$ and based on Sec. III-B, the DFT-S-OFDM-IM transmission using localized SC mapping contains the weighted superposition of M symbols, which always activate all RF chains. As a result, for SM using DFT-S-OFDM-IM with localized SC mapping, a

RF chain has to be turned on and off for the whole DFT frame, as seen in Fig. 14(a). The associated throughput is given by $R = \frac{M \log_2 L + \text{BPS}^{\text{FD-IM}} + \text{BPS}^{\text{SD-IM}}}{N}$, where the $\text{BPS}^{\text{SD-IM}} = \log_2 N_{Tx}$ bits are assigned to activate a single one out of N_{Tx} TAs. We note that if the same is applied in a SM OFDM system as seen in [62], the throughput is given by $R = \frac{N \log_2 L + \text{BPS}_{\text{Tx}}}{N}$, where the $\text{BPS}^{\text{SD-IM}}$ IM bits contribute a diminishing portion compared to $N \log_2 L$ as N increases. By contrast, the DFT size M may be substantially smaller than N.

The DFT precoding, SC mapping and N-point IFFT are conducted independently on each TA, following the procedures in Sec. II-B. After IFFT, the samples transmitted over N_{Tx} TAs are $\overline{\mathbf{x}}_n = [0 \ \cdots \ 0 \ \overline{\mathbf{x}}_n(\imath) \ 0 \ \cdots \ 0]$, where index $\imath$ carries $\text{BPS}^{\text{SD-IM}}$ IM bits in the SD. The signal received at the $\jmath$-th RAs is given by $y_n(\jmath) = \sum_{\imath=0}^{N_{Tx}-1} \sum_{\tau=0}^{N_h-1} h_\tau(\imath,\jmath) \overline{\mathbf{x}}_{<n-\tau>_N}(\imath) + v_n(\jmath)$. After FFT at each RA, the received signal modelled in the FD is given by $\overline{\mathbf{Y}}_{\overline{k}} = \sqrt{P}\overline{\mathbf{X}}_{\overline{k}}\overline{\mathbf{H}}_{\overline{k}} + \mathbf{V}_{\overline{k}}$, where we have $\overline{\mathbf{X}}_{\overline{k}} = [0 \ \cdots \ 0 \ \overline{X}_{\overline{k}}(\imath) \ 0 \ \cdots \ 0] \in \mathbb{C}^{1\times N_{Tx}}$, while the elements in the $(N_{Tx} \times N_{Rx})$-element channel matrix are given by $\overline{H}_{\overline{k}}(\imath,\jmath) = \sum_{\tau=0}^{N_h-1} h_\tau(\imath,\jmath)\omega_N^{-\overline{k}\tau}$. The MIMO MMSE FDE is applied as $\overline{\mathbf{U}}_{\overline{k}} = \overline{\mathbf{Y}}_{\overline{k}}\overline{\mathbf{G}}_{\text{MMSE}}$, where $\overline{\mathbf{G}}_{\text{MMSE}} = \frac{1}{\sqrt{P}}(\overline{\mathbf{H}}_{\overline{k}}^H \overline{\mathbf{H}}_{\overline{k}} + N_0 \mathbf{I}_{N_R})^{-1}\overline{\mathbf{H}}_{\overline{k}}^H$. The $(1\times N_{Tx})$-element $\overline{\mathbf{U}}_{\overline{k}} = [\overline{U}_{\overline{k}}(0), \cdots, \overline{U}_{\overline{k}}(N_{Tx}-1)]$ contains the MMSE estimates for each TA. Bearing in mind that there is no ICI in both SM's spatial domain and DFT-S-OFDM's frequency domain, the single-stream based ML detection may be expressed as:

Step 1 (SC demapping): $U_k^z(\imath) = \overline{U}_{k+z}(\imath)$, $0 \le k \le M-1, \ 0 \le \imath \le N_{Tx}-1$.
Step 2 (M-point IDFT): $u_m^z(\imath) = \frac{1}{\sqrt{M}} \sum_{k=0}^{M-1} U_k^z(\imath)\omega_M^{km}$, $0 \le m \le M-1, \ 0 \le \imath \le N_{Tx}-1$.
Step 3 (Demodulation): $\hat{x}_m^z(\imath) = \mathbb{M}^{-1}(u_m^z(\imath))$, $0 \le m \le M-1, \ 0 \le \imath \le N_{Tx}-1$.
Step 4 (SD-IM decision): $\hat{\imath}^z = \arg \ \min_{\forall \imath} \ d(i,z)$, where $d(i,z) = \sum_{m=0}^{M-1} \|\mathbf{u}_m^z - \hat{\mathbf{x}}_m^z\|^2$,
Step 5 (FD-IM decision): $\hat{z} = \arg \ \min_{\forall z} \ d(\hat{\imath}^z, z)$.
Step 6 (Final decisions): $\hat{\imath} = \hat{\imath}^{\hat{z}}$ and $\hat{x}_m = \hat{x}_m^{\hat{z}}(\hat{\imath})$, $0 \le m \le M-1$. (33)

The $(1\times N_{Tx})$-element row vectors in Step 4 are given by $\mathbf{u}_m^z = [u_m^z(0), \cdots, u_m^z(N_{Tx}-1)]$ and $\hat{\mathbf{x}}_m^z = [\hat{x}_m^z(0), \cdots, \hat{x}_m^z(N_{Tx}-1)]$. The detection complexity order of (33) is given by $\mathcal{O}(N_{Tx}MC^{\text{FD-IM}})$, which does not grow with the constellation size but still increases with the number of IM combinations in both the SD and FD.

In contrast to the localized SC mapping, the distributed SC mapping results in repeated and rotated PSK/QAM symbols in the TD, as demonstrated in Proposition 1 associated with $G = 1$. This implies that the sparse signal matrices modulated according to SM, GSM and ASTSK remain sparse after IFFT at the transmitter. As a result, the DFT-S-OFDM-IM using distributed SC mapping is the preferred choice for single-RF and reduced-RF MIMO schemes. The schematic of SM DFT-S-OFDM-IM using distributed SC mapping is portrayed in Fig. 14(b). The associated throughput is increased to $R = \frac{M(\log_2 L + \text{BPS}_{Tx}) + \text{BPS}^{\text{FD-IM}}}{N}$. More explicitly, after IFFT at each TA, the transmitted TD samples are given by:

$$\overline{\mathbf{x}}_n = [\ 0 \ \cdots \ 0 \ \underset{\downarrow}{\overset{\imath_{(n \bmod M)}}{\omega_N^{zn} x_{(n \bmod M)}}} \ 0 \ \cdots \ 0], \tag{34}$$

where $x_{(n \bmod M)}$ and $\imath_{(n \bmod M)}$ carry $\log_2 L$ and $\text{BPS}^{\text{SD-IM}}$ bits, respectively. For SM DFT-S-OFDM-IM using distributed SC mapping, the received signal model and the MMSE FDE follow the same procedures as discussed above for the localized SC mapping. Moreover, for the signal detection, the first steps of SC demapping and M-point IDFT are also the same as (33), except that the SC demapping index is replaced by $U_k^z = \overline{U}_{\overline{k}=kP+z}$. After IDFT, the joint detection of modulated symbols indices $\{l_m\}_{m=0}^{M-1}$, SD-IM indices $\{\imath_m\}_{m=0}^{M-1}$ and FD-IM index z may be formulated as:

$$\{\hat{l}_m\}_{m=0}^{M-1}, \{\hat{\imath}_m\}_{m=0}^{M-1}, \hat{z} = \underset{\forall\{l_m\}_{m=0}^{M-1}\forall\{\imath_m\}_{m=0}^{M-1}\forall z}{\arg \min} \sum_{m=0}^{M-1} d_m^z(l_m, \imath_m), \tag{35}$$

where we have $d_m^z(l_m,\imath_m) = \|\mathbf{u}_m^z - \mathbf{x}^{l_m,\imath_m}\|^2$. The $(1\times N_{Tx})$-element $\mathbf{x}^{l_m,\imath_m}$ is formulated by (34), where the $\imath_m$-th non-zero element is modulated as x^{l_m}. Once again, there is no ICI in both SD and FD. Therefore, the remaining detection steps are:

Step 3 (Demodulation): $\hat{x}_m^z(\imath_m) = \mathbb{M}^{-1}(u_m^z(\imath_m))$, $0 \le m \le M-1, \ 0 \le \imath \le N_{Tx}-1$.
Step 4 (SD-IM decision): $\hat{\imath}_m^z = \arg \ \min_{\forall \imath} \ d_m^z(\hat{x}_m^z(\imath_m), \imath_m)$.
Step 5 (FD-IM decision): $\hat{z} = \arg \ \min_{\forall z} \ \sum_{m=0}^{M-1} d_m^z(\hat{x}_m^z(\hat{\imath}_m^z), \hat{\imath}_m^z)$.
Step 6 (Final decisions): $\hat{\imath}_m = \hat{\imath}_m^{\hat{z}}$ and $\hat{x}_m = \hat{x}_m^{\hat{z}}(\hat{\imath}_m)$. (36)

The detection complexity order is given by $\mathcal{O}(N_{Tx}MC^{\text{FD-IM}})$.

For ASTSK DFT-S-OFDM-IM using distributed SC mapping, the sparse $(T \times N_{Tx})$ signal matrix is modulated as $x^l\mathbf{A}_q$ before DFT precoding, where the SD-TD-IM index q carries $\log_2 Q$ bits. The $(T\times N_{Tx})$-element dispersion matrices $\{\mathbf{A}_q\}_{q=0}^{Q-1}$ are optimized for the sake of achieving a diversity gain in both SD and TD [56], [57]. After the DFT precoding, SC mapping and IFFT, the ASTSK signals are transmitted in the same way as SM. The associated throughput is given by $R = \frac{(\log_2 L + \log_2 Q)M/T + \text{BPS}^{\text{FD-IM}}}{N}$. At the receiver, after the same N-point FFT, subcarrier demapping and M-point IDFT, the joint detection of modulated symbols indices $\{l_t\}_{t=0}^{M/T-1}$, SD-TD-IM indices $\{q_t\}_{t=0}^{M/T-1}$ and FD-IM index z is formulated as:

$$\{\hat{l}_t\}_{t=0}^{M/T-1}, \{\hat{q}_t\}_{t=0}^{M/T-1}, \hat{z} = \underset{\forall\{l_t\}_{t=0}^{M/T-1}\forall\{q_t\}_{t=0}^{M/T-1}\forall z}{\arg \min} \sum_{t=0}^{M/T-1} d_t^z(l_t, q_t), \tag{37}$$

where we have $d_t^z(l_t,q_t) = \|\mathbf{U}_t^z - x^{l_t}\mathbf{A}_{q_t}\|^2$ and the stacked $(T \times N_{Tx})$-element matrix $\mathbf{U}_t^z = [(\mathbf{u}_{tT}^z)^T, (\mathbf{u}_{tT+1}^z)^T, \cdots, (\mathbf{u}_{tT+T-1}^z)^T]^T$. Considering that there is still no ICI in the SD, TD and FD, similar to (36), the remaining ASTSK detection steps are:

Step 3 (Demodulation): $\hat{x}_t^z(q_t) = \mathbb{M}^{-1}\{\text{tr}(\mathbf{A}_{q_t}^H \mathbf{U}_t^z / \|\mathbf{A}_{q_t}\|^2)\}$, $0 \le t \le M/T-1, \ 0 \le q \le Q-1$.
Step 4 (SD-TD-IM decision): $\hat{q}_t^z = \arg \ \min_{\forall q} \ d_t^z(\hat{x}_t^z(q_t), q_t)$.
Step 5 (FD-IM decision): $\hat{z} = \arg \ \min_{\forall z} \ \sum_{t=0}^{M/T-1} d_t^z(\hat{x}_t^z(\hat{q}_t^z), \hat{q}_t^z)$.
Step 6 (Final decisions): $\hat{q}_t = \hat{q}_t^{\hat{z}}$ and $\hat{x}_t = \hat{x}_t^{\hat{z}}(\hat{q}_t)$. (38)

The detection complexity order is given by $\mathcal{O}(QMC^{\text{FD-IM}})$.

Fig. 15 demonstrates that firstly, when employing the same QPSK modulation and using the same DFT-S-OFDM-IM parameters, SM using DFT-S-OFDM-IM with distributed SC mapping achieves the highest $\text{BPB} = R \times N$, followed by

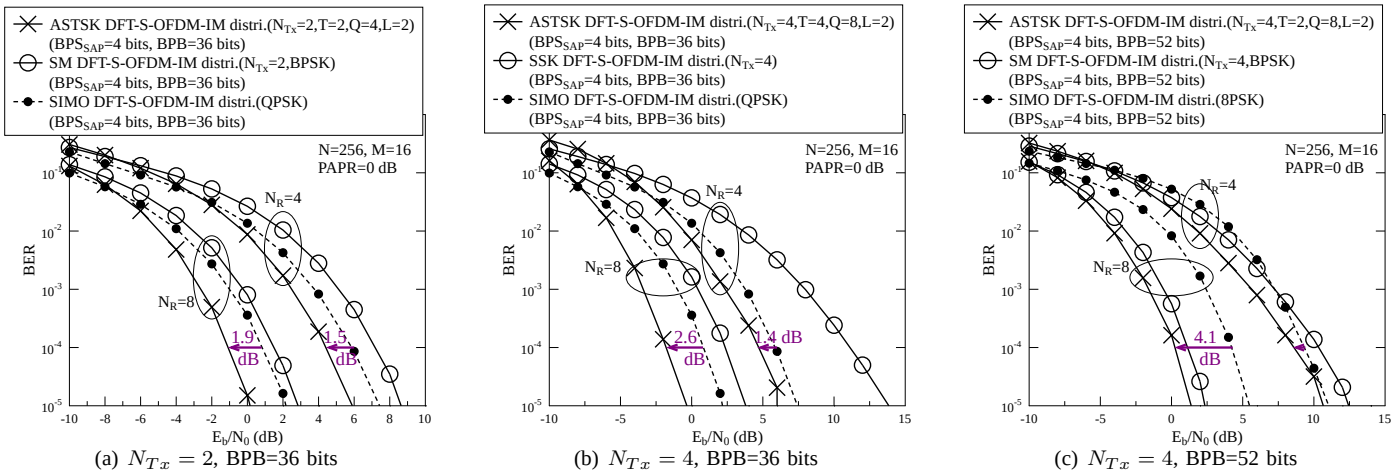

(a) $N_{Tx} = 2$, BPB=36 bits (b) $N_{Tx} = 4$, BPB=36 bits (c) $N_{Tx} = 4$, BPB=52 bits

Fig. 16: Performance comparison between SM, ASTSK and SIMO using DFT-S-OFDM-IM using distributed SC mapping, where $N = 256$ and $M = 16$ are used, and PAPR=0 dB signal transmission is ensured. The parameters and descriptions of the ASTSK schemes may be found in [57].

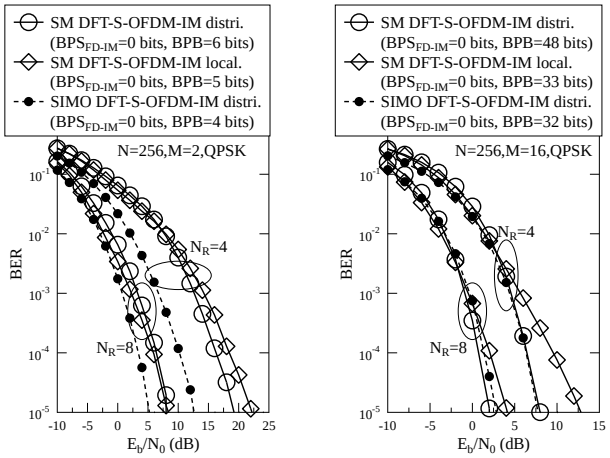

(a) $M = 2$ (b) $M = 16$

Fig. 15: Performance comparison between SM DFT-S-OFDM-IM using localized and distributed SC mapping as well as the single-TA based SIMO DFT-S-OFDM-IM, where $N = 256$, $N_{Tx} = 2$ and QPSK are used.

SM using DFT-S-OFDM-IM with localized SC mapping and SIMO using DFT-S-OFDM. Secondly, Fig. 15 shows that the performance advantage of SM DFT-S-OFDM-IM using distributed SC mapping over its localized counterpart improves as M increases. Thirdly, Fig. 15 also demonstrates that the SM schemes do not always achieve a performance gain over their SIMO counterparts, when compared at the same throughput. As a remedy, Fig. 16 confirms that ASTSK using DFT-S-OFDM-IM is capable of outperforming its SM and SIMO counterparts at the same throughput, thanks to the diversity gains obtained from all the three SD, TD and FD.

V. Conclusions

In this work, we proposed a new waveform termed as MB-DFT-S-OFDM-IM, which supports *diverse* communication requirements within a single *unified* platform. The beneficial trade-off improvements that are adjustable by configuring G are summarized in Table III. The MB-DFT-S-OFDM-IM mitigates the OFDM deficiencies of high PAPR, complex OOB filtering, bandwidth efficiency loss due to the CP overhead and sensitivity to carrier frequency offset *without compromising on the SC orthogonality*, which ensures the maximum compatibility with the existing communication systems. Furthermore, the proposed MB-DFT-S-OFDM-IM is extended to support a variety of MIMO schemes, where the IM philosophy is integrated with the space-, time- and frequency-domains to support single-/multiple-carrier single-/multiple-RF MIMO in a *unified* platform.

References

[1] L. Hanzo, M. Munster, B. J. Choi, and T. Keller, *OFDM and MC-CDMA for Broadband Multi-User Communications, WLANs and Broadcasting*. John Wiley & Sons, 2003.

[2] L. Hanzo, L.-L. Yang, E. L. Kuan, and K. Yen, *Single and Multi-Carrier DS-CDMA: Multi-User Detection, Space-Time Spreading, Synchronisation, Networking and Standards*. John Wiley & Sons, 2004.

[3] L. Hanzo and T. Keller, *OFDM and MC-CDMA: a primer*. John Wiley & Sons, 2007.

[4] S. C. Thompson, A. U. Ahmed, J. G. Proakis, J. R. Zeidler, and M. J. Geile, "Constant envelope OFDM," *IEEE Trans. Commun.*, vol. 56, pp. 1300–1312, August 2008.

[5] T. F. Rahman, C. Sacchi, S. Morosi, A. Mazzinghi, and N. Bartolomei, "Constant-envelope multicarrier waveforms for millimeter wave 5G applications," *IEEE Trans. Veh. Technol.*, vol. 67, pp. 9406–9420, Oct 2018.

[6] 3GPP Tech. Report 21.915, "Summary of Rel-15 work items," *[Online]. Available: http://www.3gpp.org/release-15*.

[7] C. Xu, N. Ishikawa, R. Rajashekar, S. Sugiura, R. G. Maunder, Z. Wang, L. Yang, and L. Hanzo, "Sixty years of coherent versus non-coherent tradeoffs and the road from 5G to wireless futures," *IEEE Access*, vol. 7, pp. 178246–178299, 2019.

[8] H. G. Myung, J. Lim, and D. J. Goodman, "Single carrier FDMA for uplink wireless transmission," *IEEE Veh. Technol. Mag.*, vol. 1, pp. 30–38, Sep. 2006.

[9] G. Berardinelli, F. M. L. Tavares, T. B. Srensen, P. Mogensen, and K. Pajukoski, "Zero-tail DFT-spread-OFDM signals," in *IEEE Globecom Workshops (GC Wkshps)*, pp. 229–234, 2013.

[10] G. Berardinelli, K. Pajukoski, E. Lahetkangas, R. Wichman, O. Tirkkonen, and P. Mogensen, "On the potential of OFDM enhancements as

TABLE III: Summary of the MB-DFT-S-OFDM-IM trade-offs on G.

Efficiency metrics		Preference on G	Basis
Bandwidth Efficiency	Throughput	Increasing G	Proposition 2, Proposition 5, Proposition 6, Fig. 6
Energy Efficiency	PAPR	Decreasing G	Proposition 1, Proposition 7, Fig. 5
	Detection complexity	Increasing G	Proposition 3, Fig. 7
	OOB radiation	Increasing G	Fig. 11
Power Efficiency	BER	Decreasing G	Proposition 4, Fig. 8
	BER with OOB filtering	Decreasing G	Fig. 11
	BER with frequency offset	Decreasing G	Fig. 12

5G waveforms," in *2014 IEEE 79th Veh. Technol. Conf. (VTC Spring)*, 2014.

[11] M. Huemer, A. Onic, and C. Hofbauer, "Classical and bayesian linear data estimators for unique word OFDM," *IEEE Trans. Signal Process.*, vol. 59, no. 12, pp. 6073–6085, 2011.

[12] V. Vakilian, T. Wild, F. Schaich, S. ten Brink, and J. Frigon, "Universal-filtered multi-carrier technique for wireless systems beyond LTE," in *2013 IEEE GlobeCom Workshops (GC Wkshps)*, pp. 223–228, Dec 2013.

[13] G. Wunder, P. Jung, M. Kasparick, T. Wild, F. Schaich, Y. Chen, S. T. Brink, I. Gaspar, N. Michailow, A. Festag, L. Mendes, N. Cassiau, D. Ktenas, M. Dryjanski, S. Pietrzyk, B. Eged, P. Vago, and F. Wiedmann, "5GNOW: non-orthogonal, asynchronous waveforms for future mobile applications," *IEEE Commun. Mag.*, vol. 52, pp. 97–105, February 2014.

[14] B. Farhang-Boroujeny and H. Moradi, "OFDM inspired waveforms for 5G," *IEEE Commun. Surveys Tut.*, vol. 18, pp. 2474–2492, Fourthquarter 2016.

[15] Y. Cai, Z. Qin, F. Cui, G. Y. Li, and J. A. McCann, "Modulation and multiple access for 5G networks," *IEEE Commun. Surveys Tut.*, vol. 20, pp. 629–646, Firstquarter 2018.

[16] E. Basar, U. Aygolu, E. Panayirci, and H. V. Poor, "Orthogonal frequency division multiplexing with index modulation," *IEEE Trans. Signal Process.*, vol. 61, pp. 5536–5549, Nov 2013.

[17] S. Dang, G. Chen, and J. P. Coon, "Lexicographic codebook design for OFDM with index modulation," *IEEE Trans. Wireless Commun.*, vol. 17, pp. 8373–8387, Dec 2018.

[18] R. Fan, Y. J. Yu, and Y. L. Guan, "Generalization of orthogonal frequency division multiplexing with index modulation," *IEEE Trans. Wireless Commun.*, vol. 14, pp. 5350–5359, Oct 2015.

[19] T. Mao, Z. Wang, Q. Wang, S. Chen, and L. Hanzo, "Dual-mode index modulation aided OFDM," *IEEE Access*, vol. 5, pp. 50–60, 2017.

[20] M. Wen, B. Ye, E. Basar, Q. Li, and F. Ji, "Enhanced orthogonal frequency division multiplexing with index modulation," *IEEE Trans. Wireless Commun.*, vol. 16, pp. 4786–4801, July 2017.

[21] M. Wen, E. Basar, Q. Li, B. Zheng, and M. Zhang, "Multiple-mode orthogonal frequency division multiplexing with index modulation," *IEEE Trans. Commun.*, vol. 65, pp. 3892–3906, Sep. 2017.

[22] J. Choi, "Coded OFDM-IM with transmit diversity," *IEEE Trans. Commun.*, vol. 65, pp. 3164–3171, July 2017.

[23] E. Basar, "OFDM with index modulation using coordinate interleaving," *IEEE Wireless Commun. Lett.*, vol. 4, pp. 381–384, Aug 2015.

[24] Q. Li, M. Wen, E. Basar, H. V. Poor, B. Zheng, and F. Chen, "Diversity enhancing multiple-mode OFDM with index modulation," *IEEE Trans. Commun.*, vol. 66, pp. 3653–3666, Aug 2018.

[25] N. Ishikawa, S. Sugiura, and L. Hanzo, "Subcarrier-index modulation aided OFDM - will it work?," *IEEE Access*, vol. 4, pp. 2580–2593, 2016.

[26] S. Sugiura, T. Ishihara, and M. Nakao, "State-of-the-art design of index modulation in the space, time, and frequency domains: Benefits and fundamental limitations," *IEEE Access*, vol. 5, pp. 21774–21790, 2017.

[27] E. Basar, M. Wen, R. Mesleh, M. Di Renzo, Y. Xiao, and H. Haas, "Index modulation techniques for next-generation wireless networks," *IEEE Access*, vol. 5, pp. 16693–16746, 2017.

[28] D. Tsonev, S. Sinanovic, and H. Haas, "Enhanced subcarrier index modulation (SIM) OFDM," in *2011 IEEE GLOBECOM Workshops*, pp. 728–732, Dec 2011.

[29] D. Tsonev, S. Sinanovic, and H. Haas, "Complete modeling of nonlinear distortion in OFDM-based optical wireless communication," *J. Lightwave Technol.*, vol. 31, pp. 3064–3076, Sep. 2013.

[30] R. Rajbanshi, A. M. Wyglinski, and G. J. Minden, "Peak-to-average power ratio analysis for NC-OFDM transmissions," in *2007 IEEE 66th Veh. Technol. Conf.*, pp. 1351–1355, Sep. 2007.

[31] L. Xiao, B. Xu, H. Bai, Y. Xiao, X. Lei, and S. Li, "Performance evaluation in PAPR and ICI for ISIM-OFDM systems," in *2014 Int. Workshop High Mobility Wireless Commun.*, pp. 84–88, Nov 2014.

[32] M. Xiao, S. Mumtaz, Y. Huang, L. Dai, Y. Li, M. Matthaiou, G. K. Karagiannidis, E. Bjrnson, K. Yang, C. I, and A. Ghosh, "Millimeter wave communications for future mobile networks," *IEEE J. Sel. Areas Commun.*, vol. 35, pp. 1909–1935, Sep. 2017.

[33] E. Bjornson, J. Hoydis, and L. Sanguinetti, *Massive MIMO Networks: Spectral, Energy, and Hardware Efficiency*. Foundations and Trends, 2017.

[34] A. M. Niknejad and H. Hashemi, *mm-Wave silicon technology: 60 GHz and beyond*. Springer Science & Business Media, 2008.

[35] T. S. Rappaport, R. W. Heath, R. C. Daniels, and J. N. Murdock, *Millimeter wave wireless communications*. Pearson Education, 2015.

[36] T. S. Rappaport, Y. Xing, O. Kanhere, S. Ju, A. Madanayake, S. Mandal, A. Alkhateeb, and G. C. Trichopoulos, "Wireless communications and applications above 100 GHz: Opportunities and challenges for 6G and beyond," *IEEE Access*, 2019.

[37] I. F. Akyildiz, J. M. Jornet, and C. Han, "Terahertz band: Next frontier for wireless communications," *Physical Commun.*, vol. 12, pp. 16–32, 2014.

[38] C. Lin and G. Y. L. Li, "Terahertz communications: An array-of-subarrays solution," *IEEE Commun. Mag.*, vol. 54, pp. 124–131, December 2016.

[39] Z. Hasan, H. Boostanimehr, and V. K. Bhargava, "Green cellular networks: A survey, some research issues and challenges," *IEEE Commun. Surveys Tuts*, vol. 13, pp. 524–540, Fourth 2011.

[40] J. Joung, C. K. Ho, K. Adachi, and S. Sun, "A survey on power-amplifier-centric techniques for spectrum- and energy-efficient wireless communications," *IEEE Commun. Surveys Tuts.*, vol. 17, pp. 315–333, Firstquarter 2015.

[41] T. Kurner and S. Priebe, "Towards THz communications - status in research, standardization and regulation," *J. Infrared, Millimeter, and Terahertz Waves*, vol. 35, pp. 53–62, Jan. 2014.

[42] K. Roberts, Q. Zhuge, I. Monga, S. Gareau, and C. Laperle, "Beyond 100 Gb/s: capacity, flexibility, and network optimization," *IEEE/OSA J. Optical Commun. Netw.*, vol. 9, pp. C12–C23, April 2017.

[43] J. Joung, C. K. Ho, and S. Sun, "Spectral efficiency and energy efficiency of OFDM systems: Impact of power amplifiers and countermeasures," *IEEE J. Sel. Areas Commun.*, vol. 32, pp. 208–220, February 2014.

[44] N. P. Lawrence, B. W. . Ng, H. J. Hansen, and D. Abbott, "5G terrestrial networks: Mobility and coveragesolution in three dimensions," *IEEE Access*, vol. 5, pp. 8064–8093, 2017.

[45] T. S. Rappaport, J. N. Murdock, and F. Gutierrez, "State of the art in 60-GHz integrated circuits and systems for wireless communications," *Proc. the IEEE*, vol. 99, pp. 1390–1436, Aug 2011.

[46] N. Benvenuto, R. Dinis, D. Falconer, and S. Tomasin, "Single carrier modulation with nonlinear frequency domain equalization: An idea whose time has comeagain," *Proc. IEEE*, vol. 98, pp. 69–96, Jan 2010.

[47] F. Pancaldi, G. M. Vitetta, R. Kalbasi, N. Al-Dhahir, M. Uysal, and H. Mheidat, "Single-carrier frequency domain equalization," *IEEE Signal Process. Mag.*, vol. 25, pp. 37–56, Sep. 2008.

[48] B. J. Jeong and H. K. Chung, "Pilot structures for the uplink single carrier FDMA transmission systems," in *IEEE Veh. Technol. Conf.*, pp. 2552–2556, May 2008.

[49] E. Basar, "On multiple-input multiple-output OFDM with index modulation for next generation wireless networks," *IEEE Trans. Signal Process.*, vol. 64, pp. 3868–3878, Aug 2016.

[50] R. Y. Mesleh, H. Haas, S. Sinanovic, C. W. Ahn, and S. Yun, "Spatial modulation," *IEEE Trans. Veh. Technol.*, vol. 57, pp. 2228–2241, July 2008.

[51] C. Xu, S. Sugiura, S. X. Ng, and L. Hanzo, "Spatial modulation and space-time shift keying: Optimal performance at a reduced detection complexity," *IEEE Trans. Commun.*, vol. 61, pp. 206–216, January 2013.

[52] R. Rajashekar, K. V. S. Hari, and L. Hanzo, "Reduced-complexity ML detection and capacity-optimized training for spatial modulation systems," *IEEE Trans. Commun.*, vol. 62, pp. 112–125, January 2014.

[53] M. D. Renzo, H. Haas, A. Ghrayeb, S. Sugiura, and L. Hanzo, "Spatial modulation for generalized MIMO: Challenges, opportunities, and implementation," *Proc. the IEEE*, vol. 102, pp. 56–103, Jan. 2014.

[54] P. Yang, Y. Xiao, Y. L. Guan, K. V. S. Hari, A. Chockalingam, S. Sugiura, H. Haas, M. D. Renzo, C. Masouros, Z. Liu, L. Xiao, S. Li, and L. Hanzo, "Single-carrier SM-MIMO: A promising design for broadband large-scale antenna systems," *IEEE Commun. Surveys Tuts.*, vol. 18, pp. 1687–1716, thirdquarter 2016.

[55] C. Xu, S. Sugiura, S. X. Ng, P. Zhang, L. Wang, and L. Hanzo, "Two decades of mimo design tradeoffs and reduced-complexity MIMO detection in near-capacity systems," *IEEE Access*, vol. 5, pp. 18564–18632, 2017.

[56] S. Sugiura, S. Chen, and L. Hanzo, "Coherent and differential space-time shift keying: A dispersion matrix approach," *IEEE Trans. Commun.*, vol. 58, pp. 3219–3230, November 2010.

[57] C. Xu, T. Bai, J. Zhang, R. G. Maunder, S. Sugiura, Z. Wang, and L. Hanzo, "Constant-envelope space-time shift keying," *IEEE J. Sel. Topics Signal Process.*, vol. 13, no. 6, pp. 1387–1402, 2019.

[58] C. Xu, S. Sugiura, S. X. Ng, and L. Hanzo, "Reduced-complexity non-coherently detected differential space-time shift keying," *IEEE Signal Process. Lett.*, vol. 18, pp. 153 –156, Mar. 2011.

[59] S. Sugiura, C. Xu, S. X. Ng, and L. Hanzo, "Reduced-complexity coherent versus non-coherent QAM-aided space-time shift keying," *IEEE Trans. Commun.*, vol. 59, pp. 3090–3101, November 2011.

[60] S. Sugiura, S. Chen, and L. Hanzo, "Generalized space-time shift keying designed for flexible diversity-, multiplexing- and complexity-tradeoffs," *IEEE Trans. Wireless Commun.*, vol. 10, pp. 1144–1153, April 2011.

[61] S. Sugiura, C. Xu, S. X. Ng, and L. Hanzo, "Reduced-complexity iterative-detection-aided generalized space-time shift keying," *IEEE Trans. Veh. Technol.*, vol. 61, pp. 3656–3664, Oct 2012.

[62] T. Datta, H. S. Eshwaraiah, and A. Chockalingam, "Generalized space-and-frequency index modulation," *IEEE Trans. Veh. Technol.*, vol. 65, pp. 4911–4924, July 2016.

[63] M. Wen, X. Cheng, M. Ma, B. Jiao, and H. V. Poor, "On the achievable rate of OFDM with index modulation," *IEEE Trans. Signal Process.*, vol. 64, pp. 1919–1932, April 2016.

[64] R. Rajashekar, C. Xu, N. Ishikawa, L. Yang, and L. Hanzo, "Multicarrier division duplex aided millimeter wave communications," *IEEE Access*, vol. 7, pp. 100719–100732, 2019.

[65] Y. Ko, "A tight upper bound on bit error rate of joint OFDM and multi-carrier index keying," *IEEE Commun. Lett.*, vol. 18, pp. 1763–1766, Oct 2014.

[66] S. Dang, G. Ma, B. Shihada, and M. Alouini, "A novel error performance analysis methodology for OFDM-IM," *IEEE Wireless Commun. Lett.*, vol. 8, pp. 897–900, June 2019.

[67] B. Farhang-Boroujeny, "Ofdm versus filter bank multicarrier," *IEEE Signal Processing Magazine*, vol. 28, pp. 92–112, May 2011.